

The detection by sonar of difficult targets (including centimetre-scale plastic objects and optical fibres) buried in saturated sediment

T.G. Leighton ^{*}, R.C.P. Evans

Institute of Sound and Vibration Research, University of Southampton, Highfield, Southampton SO17 1BJ, UK

Received 26 April 2006; received in revised form 19 April 2007; accepted 3 May 2007

Available online 12 July 2007

Abstract

This paper reports on a laboratory study into the use of sonar to detect objects, two of which exhibit a poor acoustic impedance mismatch with the water-saturated sediment in which they are buried to depth of about 30 cm. The targets are solid cylinders having diameters of 20–25 mm and 50 cm length, made of polyethylene, of telecommunications optical fibre, and of steel. Steel spheres are included for comparison. A poor acoustic impedance mismatch between the target and the host sediment is one factor that can make buried targets difficult to detect with sonar, but such detection is increasingly becoming an issue in a range of applications from archaeology to defence to telecommunications. Attention is paid to those signal processing techniques which could be of potential benefit. For this range of test objects, comparisons are made between use of optimal filtering and synthetic aperture sonar. In addition, the potential of a range of acousto-optical effects (optical time domain reflectometry, Raman and Brillouin scattering, and fibre optic hydrophones) is assessed in the [Appendix](#) for the particular application of detecting non-metallised fibre optic telecommunications cables. A web page dedicated to this paper hosts movies and reports at http://www.isvr.soton.ac.uk/fdag/uaua/target_in_sand.htm.

© 2007 Elsevier Ltd. All rights reserved.

Keywords: Sonar; Sediment; Seabed; Plastic target; Optical fibre

1. Introduction

This paper outlines a laboratory-based experimental investigation into the acoustic detection of difficult objects, having dimensions of a few centimetres, which are buried in underwater sediment. A key parameter in the detection of such objects is the signal-to-noise ratio (SNR). Several factors influence this, including the range, the size of the target with respect to the wavelength, the level of noise, reverberation and clutter in the received signal, the detection of resonances, the beam properties, the target strength and scattering cross-section, which in turn are influenced

by the acoustic impedance mismatch between the target and the sediment. In the field, such studies have relevance to the detection of certain types of mines [1–15] and pipelines [16,17], archaeological objects [18,19], and submarine optical fibre telecommunication cables [20]. Such cables may be buried to depths of ~ 1 m in sediment under 1 km of water. They need to be detected when repair is required, and this is currently achieved by equipping remotely operated vehicles with magnetometers which respond to the metallised cores of current commercial submarine fibre optic communications cables [20,21]. However future generations of these cables are likely to lack such metallised elements. Whilst the exploitation of acoustics in oceanographic detection has a long and successful history, such cables would represent difficult targets, indeed making the problem of detecting optical fibres buried in saturated sand akin to detecting ‘glass in glass’ using acoustics.

^{*} Corresponding author.

E-mail address: tgl@soton.ac.uk (T.G. Leighton).

URL: http://www.isvr.soton.ac.uk/FDAG/uaua/target_in_sand.HTM (T.G. Leighton).

There is a wide range of possible deployments for sonar detecting buried targets including monostatic, bistatic and multistatic systems, and platforms ranging from surface vessels to autonomous or remotely operated vehicles (in the water column or driven along the seabed). The experiment described here uses a bistatic system with the transducers close to the seabed (as would happen if they were mounted on a remotely-operated or an autonomous vehicle which travels on the seabed [20] or just above it, or on a raft in very shallow water [19]). The principles that these experiments illustrate (in terms of the propagation of the acoustic beam in the sediment and the signal processing techniques) are applicable to the general problem of the detection of objects buried in sediment. The Appendix deals specifically with alternative techniques which might be used for the particular case of detecting optical fibre telecommunications cables.

2. Materials

2.1. The saturated sediment

A steel test tank, measuring 150 cm × 180 cm × 125 cm deep, was mounted on a series of wooden blocks to reduce vibration-induced background noise. It was part-filled with 2400 kg of sediment to a depth of 50 cm, and fresh water to give a total fill-depth of 116 cm. The sediment consisted of round-grained quartz sand (BS 1200 – Fig. 1), which has less rigidity and attenuation than angular-grained natural sands [22–24]. This is a suitable analogue for seabeds at water depth of 1000 m, which are typically composed of fine sand and clay-silt, with a mean particle diameter of

less than 100 μm [25]. The size distribution of the test tank sand is shown in Fig. 2, as measured by laser scattering [26]. The density of a sample of individual sand grains was measured to be 2670 kg m⁻³ ± 2.5%, and the water-saturated sediment density was 2110 kg m⁻³ ± 2.5%, with a calculated porosity of around 0.33 (which is typical for sediments of this type [27]).

There are many examples of sediment at 1 km depth where gas bubbles do not significantly affect the acoustics, as the rate of biological out-gassing is very low [28]. However laboratory test tanks are far more prone to the presence of unwanted bubbles where they can dominate the acoustic results [29], and so a variety of stringent measures was put in place to prevent this happening [26]. These included the installation of a ‘fluidised bed’ [26,30]. In this, a constant stream of water passes through the fixed sediment bed at a speed below the limit of stability, which marks the transition to the fluidised state. This stream provides sufficient agitation to remove bubbles. A small water pump (44 m head, 40 l/min peak flow rate) was used to force the stream of water up through the sediment (Fig. 3). A nylon mesh filter was fixed over the inlet to prevent sand in suspension from entering the pump, as this would have caused damage. Water was transported in a 20 mm diameter plastic conduit and expelled through a series of approximately one hundred 1.5 mm diameter holes. The far end of the conduit was periodically opened (i.e., once every time the system was used) to flush out any sand that had accumulated. To prevent out-gassing as a result of the natural breakdown of biological material in the sediment, a small quantity of household bleach was added to the water in the laboratory tank every few months.

2.2. Acoustic propagation characteristics

The acoustic detection system required sound to propagate through clear water, water containing suspended material, and sediment before interacting with a buried object. The return path also contains such environments. Hence, it was necessary to investigate each component of the acoustic path separately to gain an understanding of the processes affecting the performance of the system as a whole (so that, for example, scatterer positioning algorithms from time-of-flight measurements could be implemented). This characterisation is detailed in Ref. [26]. From the transmission of a single-cycle sine wave pulse (of centre frequency of 75 kHz) along arrays of hydrophones in the water column and the sediment, sound speeds were estimated to be 1478 m s⁻¹ ± 2% in water and 1692 m s⁻¹ ± 2% for the pressure wave in the sediment (as indicated by the path of the fastest perturbation throughout this paper – see Section 2.5.2). These values were taken for a water temperature of 16.5 ± 0.5 °C, and an atmospheric pressure of 100.6 ± 0.05 kPa.

The effect of suspended sediment on attenuation and sound speed (and related effects such as refraction) in the water column were found to be negligible for the measure-

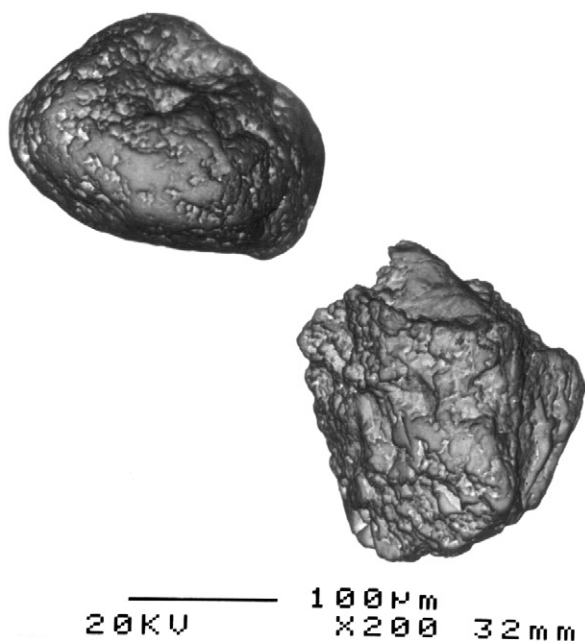


Fig. 1. A scanning electron microscope picture of two typical sand grains taken from the sediment bed. The scale bar is 100 μm in length. Microanalysis showed the particles to be principally composed of silicon and oxygen.

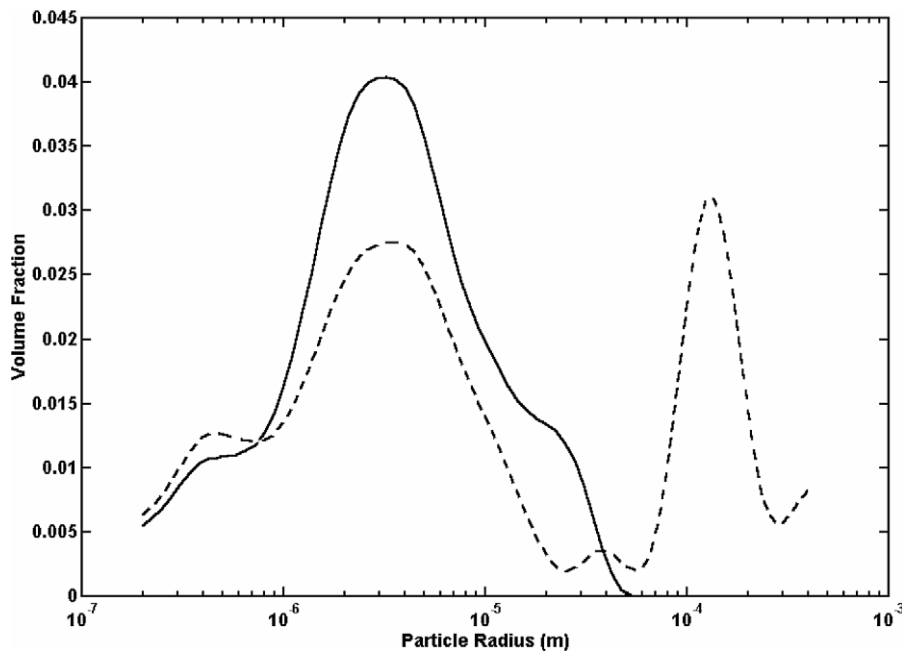


Fig. 2. The measured size distributions of sand particles in a light suspension in the water above the sediment (solid curve), and from a few centimetres beneath the surface of the sediment in the laboratory tank (dashed curve).

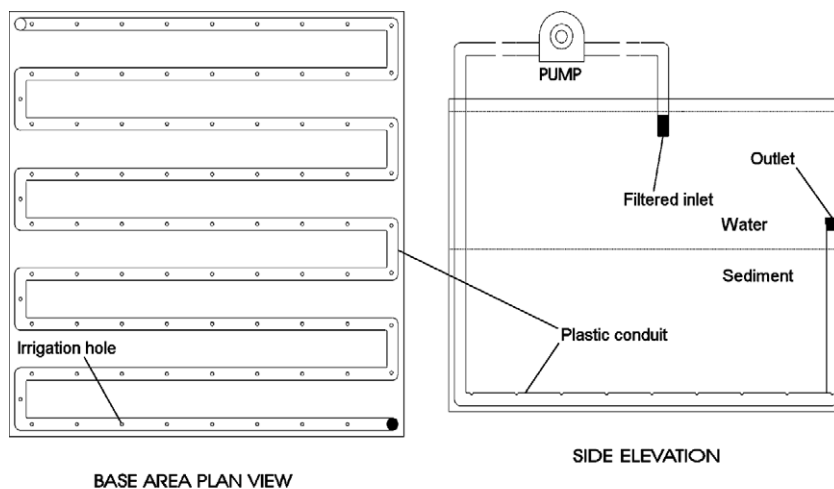


Fig. 3. Schematic layout of the fluidisation system. Bubbles were removed from the sediment by a stream of water, pumped into the conduit and expelled through the irrigation holes.

ment tolerances of the system [26]. Measurement of the attenuation of the pressure wave in this sediment provided an interesting dataset in the frequency range 10–100 kHz (the frequency range that is of particular interest in this investigation), a region in which historically measurements of attenuation in sandy saturated sediments have been more scarce than for some other frequency ranges (Fig. 4). This was done using a 1 ms long chirp pulse, sweeping upwards in frequency from 20 kHz to 150 kHz, which was used to drive the acoustic source. A $1/10$ cosine-tapered window was applied to minimise transient distortion, resulting in the useful frequency range of the pulse being reduced to 33–137 kHz. The duration of the

pulse was chosen to be as long as possible before reflections within the tank would have become a problem (determined using techniques illustrated in Section 2.5.2).

2.3. Transducer design

A bistatic acoustic sensing system (where the source and receiver are at two different locations) was chosen for ease of use in the laboratory. However the techniques utilised in this paper would in principle work in the monostatic arrangements (where the source and receiver are co-located) that have been historically favoured in active sonar. To obtain good signal-to-noise (SNR) in the scatter,

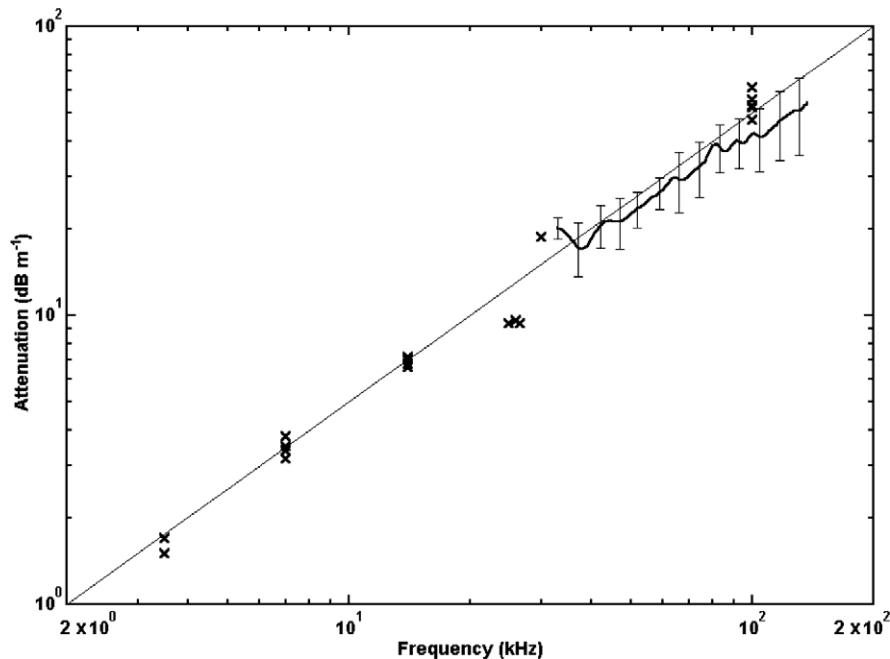


Fig. 4. The attenuation coefficient α_{dB} (in dB m^{-1}) measured in a range of saturated sandy marine sediments. The average attenuation coefficient measured in the laboratory sand used in this experiment is marked by the curve. The error bars at selected frequencies correspond to ± 1 standard deviations. The points \times indicate the attenuation coefficient measured for a range of naturally occurring sandy sediments (these may be compared with attenuation coefficients of other types of sediments using Fig. 9 of Ref. [26]), compiled with data from Hamilton [22–24]. The straight line corresponds to an attenuation coefficient of $\alpha_{dB} = 0.5f_k^1$, where f_k is the acoustic frequency in kilohertz. The extent to which a power law accurately describes attenuation in saturated sediments, and across what frequency range, is discussed in the literature [27,31–33].

a high acoustic source power, and a narrow beamwidth (in both transmitter and receiver), were specified.

A remote receiver system was chosen, so that the acoustic target detection could be non-invasive (although preliminary measurements to characterise the in-sediment propagation and validate the performance of the remote hydrophones used buried sensors – see Section 2.5). The remote hydrophone system will be discussed more fully in Section 3.1.

The sensing volume was defined by the overlap of the beampatterns of the transmitter and remote receiver [26]. Certain options were considered and rejected [26]. These included the use of: parametric sonar [34] (rejected on grounds of power and limited interaction distance in a small tank); beamforming [35] (rejected on grounds of the cost of generating a sufficiently large and windowed array to compromise between directionality and sidelobe generation), [36]; and iterative, time-reversal focusing [37] (rejected because of high attenuation in the sediment).

Instead a system based on the use of acoustic reflectors was chosen, primarily for its simplicity and low cost, and suitability for use in a small tank. This system allows directionality to be obtained from a single omni-directional transducer placed on the acoustic axis of a curved focusing acoustic reflector. Whilst inexpensive, electronic beamsteering (a simple procedure if beamforming is used) was not possible. Instead transducer/reflector assembly was repositioned *en masse* using a custom-built computer-controlled positioning rig [26]. The focal length of the transducer/

reflector assembly was varied by changing the position of the source relative to the back of the reflector [26].

Of the options available (paraboloidal, spherical wave, ellipsoidal and hyperboloidal [38]), a spherical reflector was chosen because it was the easiest to fabricate to the required a surface tolerance of much less than a wavelength. In addition, the effect on the acoustic field of a spherical reflector is very similar to the effect of a parabolic one in the paraxial focusing region and, in general, will suffer less aberration than its aspheric counterparts [26]. The maximum reflector size was constrained by the dimensions of the laboratory tank and, to some extent, by the cost of fabrication. After comparing by simulation the performance of a range of reflectors of various sizes [26] in terms of compromising between focusing, aberrations and the practical limitations placed on source positions, two 35 cm diameter spherical reflectors (one for the transmitter, and one for the receiver) were cut from a block of closed-cell expanded polyurethane foam (a pressure-release surface underwater). This cutting was done to a surface tolerance of ± 1 mm, i.e., around 1/20 of an acoustic wavelength at 75 kHz in water [26].

Calibrated Brüel & Kjær type 8103 hydrophones were used as both the acoustic source and receiver elements (the variation in hydrophone sensitivity should have been less than 3 dB in every direction at a frequency of 100 kHz [39], and less than this at lower frequencies). In order to confine their directional responses to within the collection angles of the reflectors, back-reflectors were

attached to each of the hydrophones (their effectiveness is discussed in Section 2.5.2).

Fig. 5 demonstrates the performance of the transmitter (i.e. hydrophone source and reflector) in the free field (time-gated in an $8\text{ m} \times 8\text{ m} \times 5\text{ m}$ deep water tank) with the hydrophone fixed 13 cm from the back of the reflector such that the paraxial focus was, in theory, close to infinity. That hydrophone, which was used as an acoustic projector, was driven by a series of single-cycle sine wave pulses, each having a centre frequency of 75 kHz. The 3 dB bandwidth of such a pulse extends from 31.1 kHz to 98.0 kHz. If the response of the hydrophone (which was found to have a peak at around 120 kHz when used as an acoustic source) is also taken into consideration, then most of the transmitted acoustic energy is found to lie between 75 kHz and 100 kHz [26]. The acoustic pressure amplitude that resulted from each pulse was recorded at discrete points in front of the reflector using an independent hydrophone.

The measured sound field is shown in Fig. 5. The SPL at each of the sample points, \times , is calculated from the pulse-averaged intensities measured at the receiver relative to $1\text{ }\mu\text{Pa rms}$ [26,40]. A continuous image was obtained using piecewise, bilinear interpolation between the sampling points. The solid outline delineates the theoretical boundary of the acoustic field, i.e., the back of the reflector and the caustic.

It can be seen from Fig. 5 that the highest energy density coincides with the point at which marginal rays cross the acoustic axis [26]. From Fig. 5, the directivity index (the ratio of the intensity of a directional source at some distance

on the acoustic axis to the intensity of an omni-directional source at the same distance) of the focused acoustic reflector was estimated to be greater than 20 dB [26].

Following this free-field characterisation, the propagation of the beam into the sediment was measured. Care was also taken to ensure that the water–sediment interface displayed translational invariance, or stationarity, such that the statistics of one section of the surface were the same as the statistics of a different section of the same surface [26,41–43]. Within the footprint made by the beam on the sediment/water interface, there will be a certain roughness. Obviously if any departures from a smooth surface are much smaller than a wavelength, the surface can be considered to be acoustically smooth. However the simple assumption that the roughness increases with increasing frequency is not necessarily true for all acoustic systems, because for a transmitter of a given size, the directionality will be frequency-dependent and so too will be the size of the footprint: the apparent roughness for an individual ‘ping’ may decrease if an increase in frequency reduces the footprint size. Furthermore, if a pulse is used, the ‘footprint’ will take the form of a time-varying area on the interface, the size of which may reduce if the pulse duration decreases [44,45].

2.4. Surface roughness

Data for two angles of incidence θ_i ($64^\circ \pm 2^\circ$ and $33^\circ \pm 2^\circ$, corresponding to respective grazing angles θ_g of $26^\circ \pm 2^\circ$ and $57^\circ \pm 2^\circ$; see Fig. 6) and two surface rough-

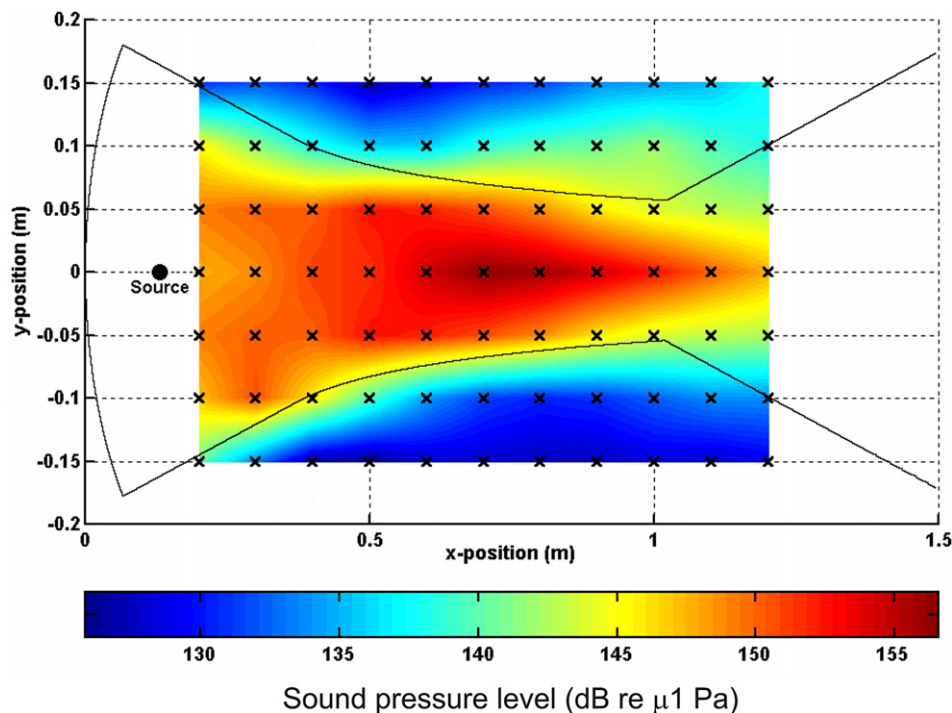


Fig. 5. The experimentally measured sound field generated by a focused acoustic reflector (focusing at ∞) in water in the free field. The crosses represent discrete measurement positions and the solid line delineates the theoretical boundary of the acoustic field (which on the left side corresponds to the surface of the reflector).

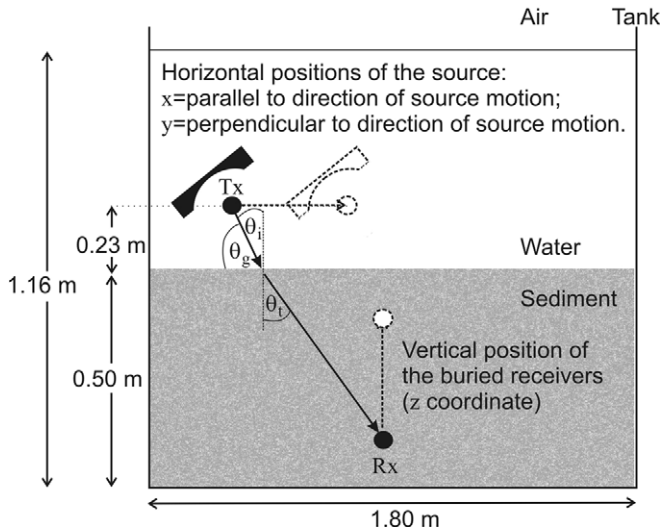


Fig. 6. The source/receiver arrangement for the sediment transmission loss measurement in the laboratory tank. The filled symbols represent the initial positions of the acoustic source, Tx, and receiver, Rx. The outlined symbols represent the range of positions of Tx and Rx. The figures show the angles of incidence (θ_i) and transmission (θ_t), measured between transducer axis and normal to the mean horizontal sediment reference plane; and the grazing angle (θ_g), measured between transducer axis and the mean horizontal sediment reference plane. It is recognised that finite beam pattern and surface roughness mean that not all of the acoustic energy is restricted to these nominal angles.

nesses are reported in this paper. The surface characteristics were as follows:

- *The 'smooth' interface:* For all the measurements described in this paper, with the exception of Fig. 8, a 'smooth' interface was used. Its topography was characterised by taking 20 depth measurements at random positions using a plumb-line. The measured rms height variation was less than the error associated with the use of the plumb-line, which was estimated to be ± 1 mm. Therefore, the rms height was taken to be $\Delta h_s < 1$ mm. Therefore the maximum value of the Rayleigh roughness parameter $R_a = k\Delta h_s \sin\theta_g$ (found for $\Delta h_s = 1$ mm using the acoustic wavenumber k in water corresponding to 100 kHz – see above), for a grazing angle of $57^\circ \pm 2^\circ$, is $R_a = 0.35 \pm 0.01$. A surface is considered to be 'rough' if $R_a > 2\pi/8 > \sim 0.8$. Hence values of R_a are small enough to classify the interface as 'smooth'.
- *The 'rough interface':* In addition to the 'smooth' surface discussed above, tests were made of a 'rough' surface which was fashioned using a weighted corrugated strip that was dragged across the width of the laboratory tank. The strip profile was sinusoidal with a period of 3.2 cm and an rms height of 6.4 mm. (It should be noted that the imposed roughness was not random since all of the corrugations were parallel). After dragging, a small quantity of fine sediment was observed to have been swept up into suspension and settled out over the next few hours. The plumb-line was used to measure the

surface roughness by taking 20 equally spaced measurements in the direction of the sinusoidal profile. The rms height was confirmed to be 6.4 mm with an error of ± 1 mm. This paper reports on results with this 'rough' surface for a grazing angle θ_g of $26^\circ \pm 2^\circ$ only, for which the Rayleigh roughness parameter takes a value of 0.89 ± 0.16 at a frequency of 75 kHz, and 1.17 ± 0.20 at 100 kHz. Both values of R_a are large enough to classify the interface as 'rough'.

2.5. Preliminary characterisation of acoustic penetration

This section reports on results from two of the preliminary tests undertaken to characterise the acoustic penetration of the sediment by the beam. One reason for undertaking such tests was to validate the results of using a remote receiving system (as will be described in Section 3.1, Fig. 10), by first taking data using buried hydrophones. The apparatus would not allow continuous variation in the grazing angle, and the two values chosen are those closest to the ideal angles. In Section 2.5.2, a grazing angle of $26^\circ \pm 2^\circ$ is used to examine the effect near the critical angle [41,46]. Before that, Section 2.5.1 will report on tests with a grazing angle of θ_g of $57^\circ \pm 2^\circ$ (i.e., and angle of incidence θ_i of $33^\circ \pm 2^\circ$), which was used for all the tests of Sections 3 and 4 because, as will now be explained, it gives optimal coverage.

2.5.1. Beam plot in sediment for smooth interface and $33^\circ \pm 2^\circ$ angle of incidence

The target detection tests, which will be described in Sections 3 and 4, will all use the 'smooth' interface and an angle of incidence θ_i of $33^\circ \pm 2^\circ$. Therefore the acoustic penetration for sediment/beam system was characterised. In this subsection, results are shown for penetration close to the critical angle, to illustrate the method. A two-dimensional measurement was obtained by moving the receiver vertically (i.e., in the z -direction) within the sediment and the reflector horizontally above it (the direction of movement being used to define the x -direction; see Fig. 6). This technique is valid if the statistics of the beam footprints are invariant from one location to the next. An error of ± 1 dB was determined for the error associated with use of inserted hydrophones, which are calibrated for use in water. The height of both above the sediment surface was $23 \text{ cm} \pm 1 \text{ cm}$, close to the 25 cm required (from calculations based on the free field beam pattern of Fig. 5) to maximise the peak sound pressure that would occur at a depth of 25 cm beneath the sediment surface. The angle at which the acoustic axes of both transmitter and receiver met the normal to the reference plane of the sediment interface was $33^\circ \pm 2^\circ$ (the angle of incidence θ_i ; see Fig. 6). This angle is close to the 30° which, it was calculated, would give optimal coverage of the sediment volume in range and in depth (the angle of incidence could not be adjusted continuously over the range) [26]. Simple application of Snell's

law predicts an angle of propagation in the sediment of $38.6^\circ \pm 2.8^\circ$, which agrees with the measured value $37^\circ \pm 2^\circ$ obtained in Fig. 7 when the acoustic projector was driven by a series of single-cycle sine wave pulses, each having a centre frequency of 75 kHz (see Sections 2.2 and 2.3).

2.5.2. Effect of surface roughness, and measurement of sound speeds

Whilst the target detection experiments (to be described in Sections 3 and 4) were conducted using the ‘smooth’ surface (which had an rms roughness of <1 mm as described in Section 2.4), preliminary tests were made to characterise the effect of varying surface roughness on this test sediment bed. The results for measurements using a grazing angle of $26^\circ \pm 2^\circ$ are shown, to examine the effect near the critical grazing angle (which is $29^\circ \pm 3^\circ$ for a measured sediment sound speed of 1692 ± 34 m s⁻¹ and a measured water sound speed of 1478 ± 30 m s⁻¹). Of course, whilst the source produced waves close to planar on axis, there was a beam pattern (Fig. 5) and this, along with the existence of any surface corrugations, means that not all of the acoustic energy will be incident on the sediment at the nominal $26^\circ \pm 2^\circ$ grazing angle.

The average acoustic pressure amplitude as a function of time was measured at each position of the source and buried hydrophone. (The average was calculated from 1000 measurements at each position although, given the low

noise conditions in the laboratory, this amount of averaging was excessive). By plotting the two-dimensional sound field at discrete moments in time, it was possible to visualise the progression of compressional acoustic waves within the sediment.

Fig. 8 compares the pressure in the sediment obtained from the smooth (upper plot) and rough (lower plot) interfaces, at six times t_e measured after the initial excitation of the source hydrophone. As expected for conditions close to the critical angle, the beam axis propagates almost parallel to the interface. In each plot, a weak emission can be seen propagating ahead of the main pulse (for example Fig. 8c, at $t_e = 750$ μ s, it intersects the sediment/water interface at a horizontal displacement of between 0.8 m and 0.9 m from the source transducer). This arises from the direct transmission of sound from the source hydrophone without reflection from the spherical reflector, because the source hydrophone is not perfectly shielded in this direction. For practical purposes it does not enter into the analyses in this paper because its amplitude is more than 30 dB below that of the focused plane wave (which in Fig. 8c intersects the water/sediment interface at a displacement of ~ 0.57 m).

As t_e increases it becomes increasingly clear from visual inspection of Fig. 8 that more acoustic energy is transmitted through the rough interface than through the smooth interface, and penetrates to greater depths. This is quantified in Fig. 9. However the data in Fig. 9 must be treated with caution after about $t_e = 800$ μ s. This is because the

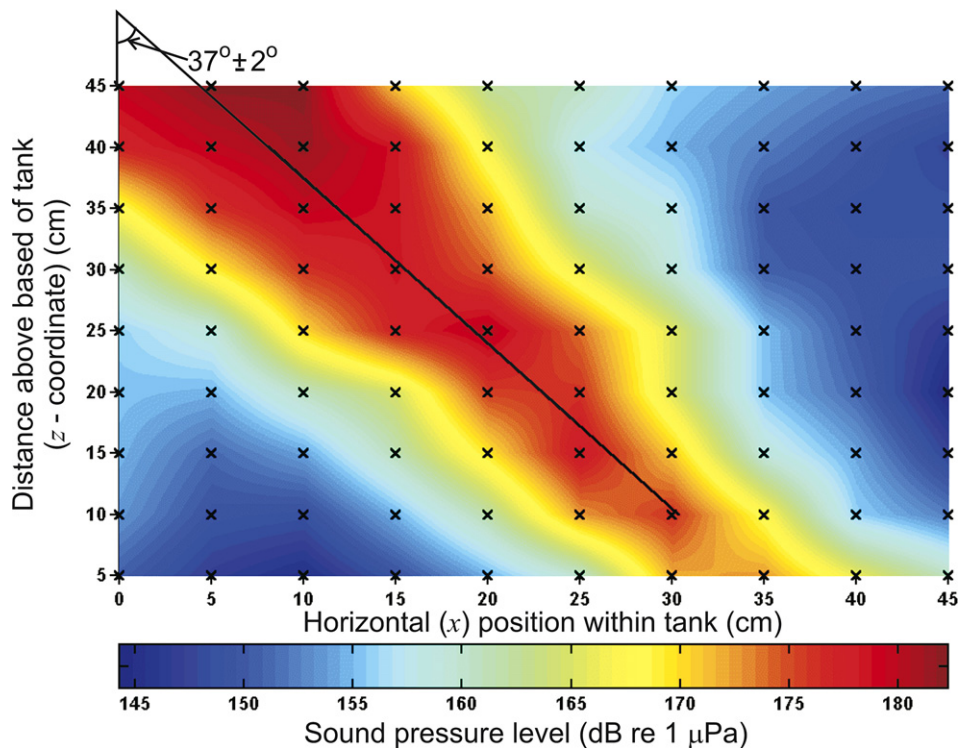


Fig. 7. The sound field generated within the ‘smooth’ sediment bed by a focused acoustic reflector for an angle of incidence at the water/sediment interface of $33^\circ \pm 2^\circ$. The crosses represent discrete measurement positions, the other data being interpolations between these. The solid line indicates the calculated position of the acoustic axis (see [26]).

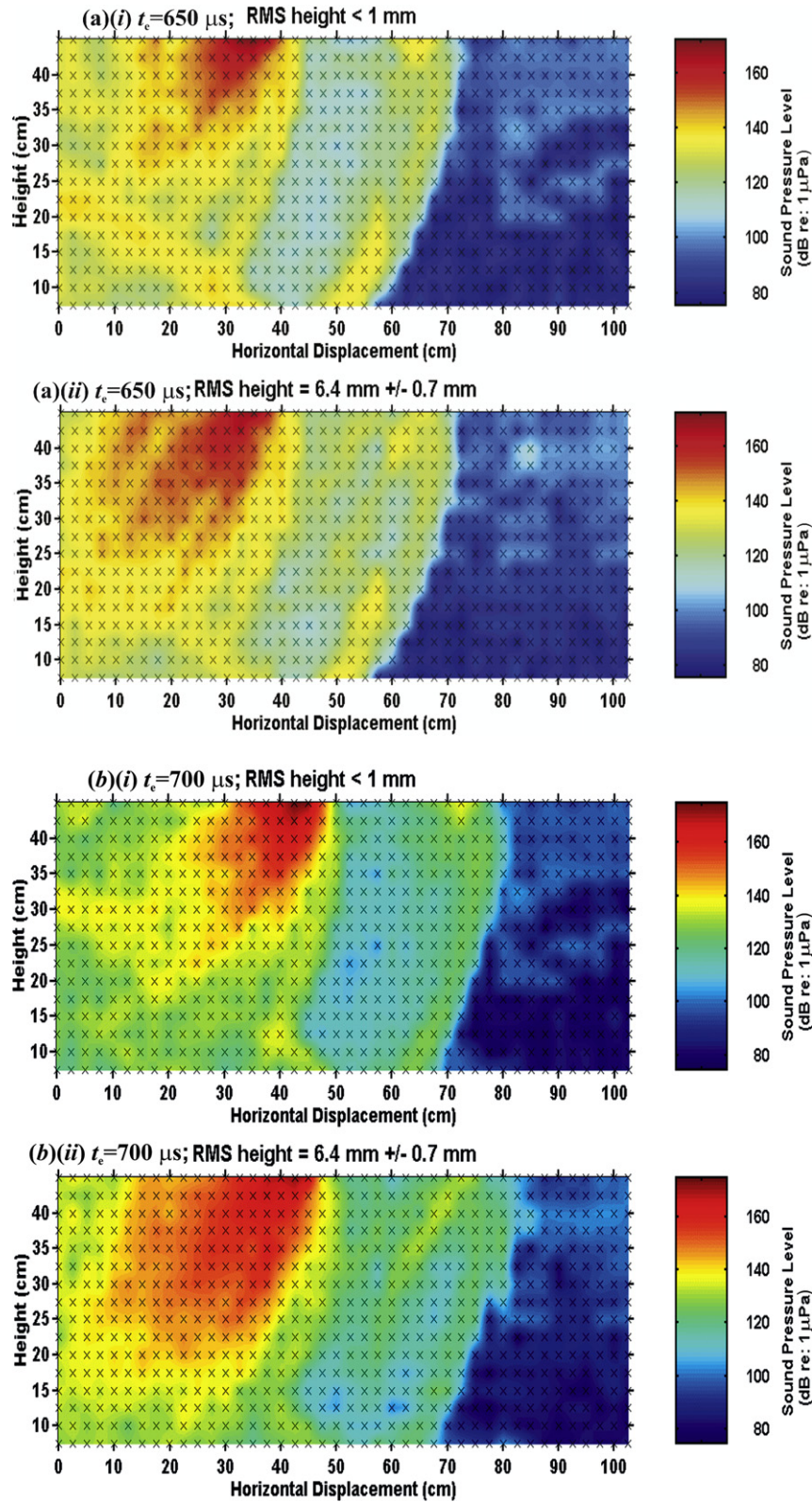


Fig. 8. The sound field within the laboratory sand at an elapsed time after the excitation of the source hydrophone of (a) 650 μs, (b) 700 μs, (c) 750 μs, (d) 800 μs, (e) 850 μs, (f) 900 μs. For each panel the upper plot (i) corresponds to the ‘smooth’ interface (rms height < 1 mm) and the lower plot (ii) corresponds to the ‘rough’ interface (rms height 6.4 ± 0.7 mm). The upper surface of the sediment is at 50 cm height on the mantissa, and the base of the tank corresponds to 0 cm on the mantissa.

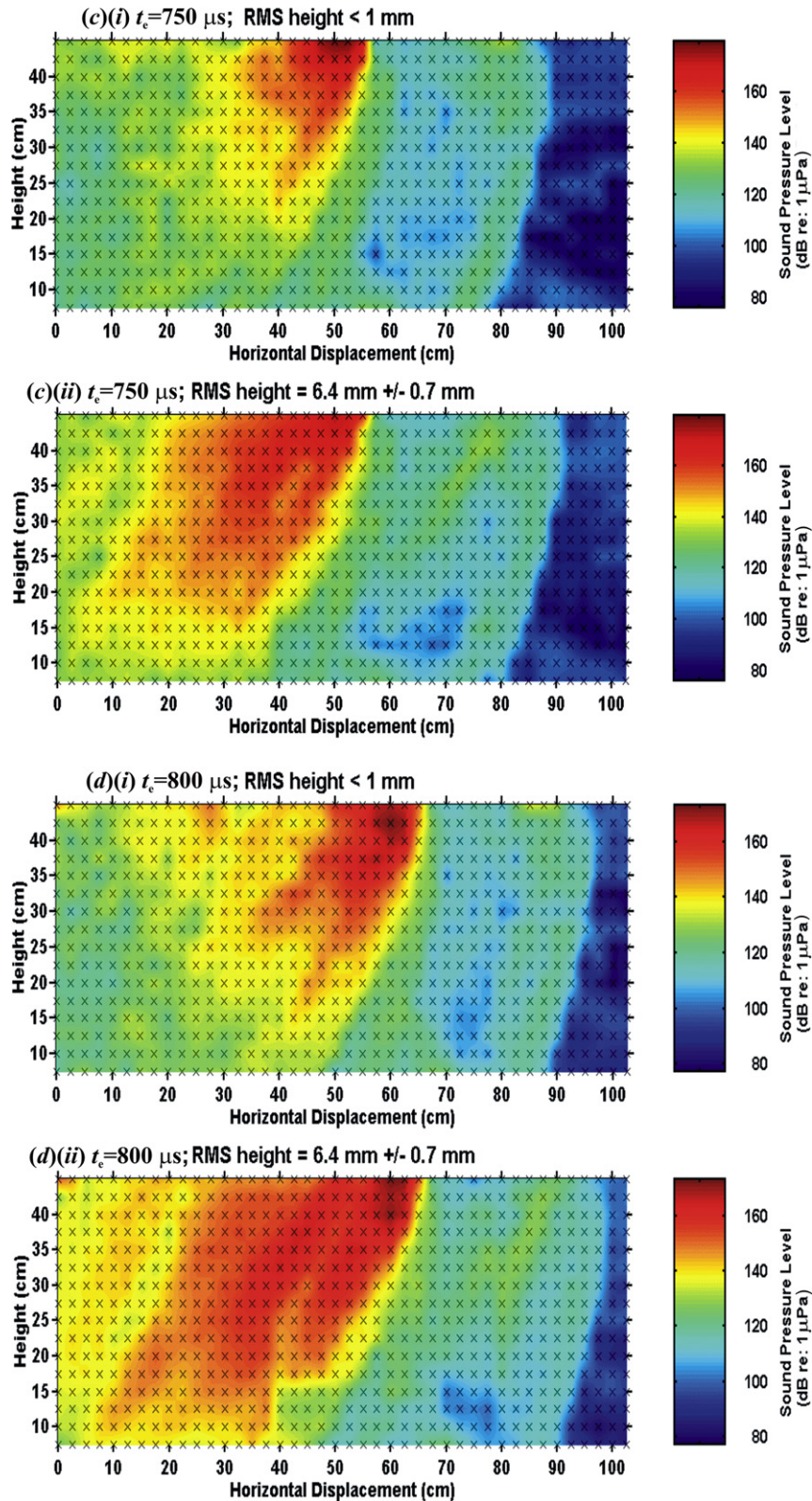


Fig. 8 (continued)

incident energy begins to interact with the tank base at $t_e = 800 \mu\text{s}$ (Fig. 8d), and at $t_e = 850 \mu\text{s}$ (Fig. 8e) the arrival of the first reflection of a source sidelobe from the water/air surface is seen to enter the top left corner of the frame.

The data in Fig. 9 show increased acoustic penetration of the rough sediment surface compared to that of the smooth one, not only of the acoustic pulse generated by the source but also of the background noise (see Fig. 9

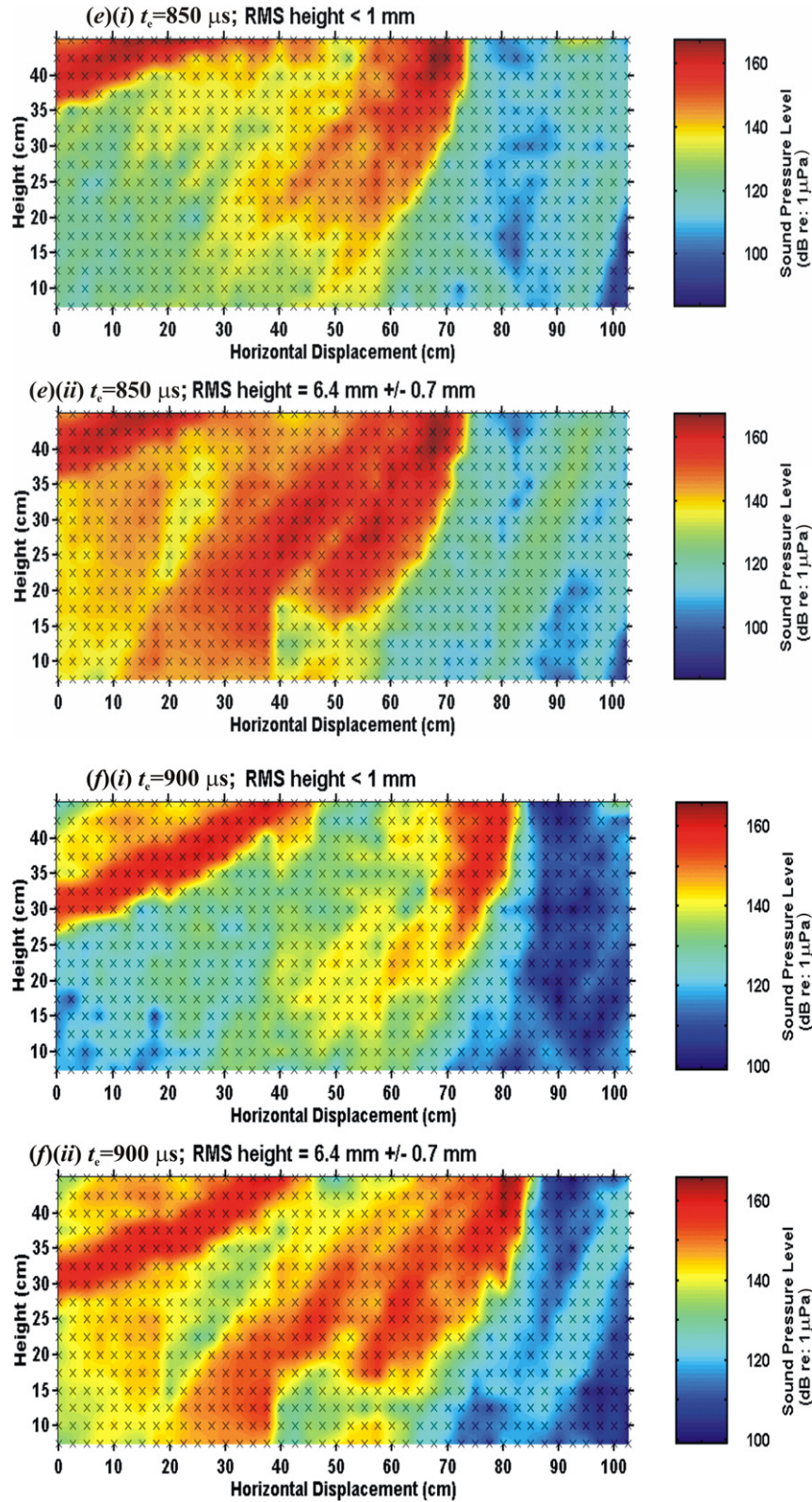


Fig. 8 (continued)

for $500 \mu\text{s} < t_e < 650 \mu\text{s}$). Wave interactions at the sediment interface [43,47–54], and particularly the enhanced penetration associated with rough surfaces [41,43,55–67] are interesting topics in their own right. However this topic will not

be explored further in this paper. Instead, having demonstrated the ability to conduct preliminary characterisation of the acoustic penetration of the sediment, the remainder of this current paper will explore the acoustic detection of

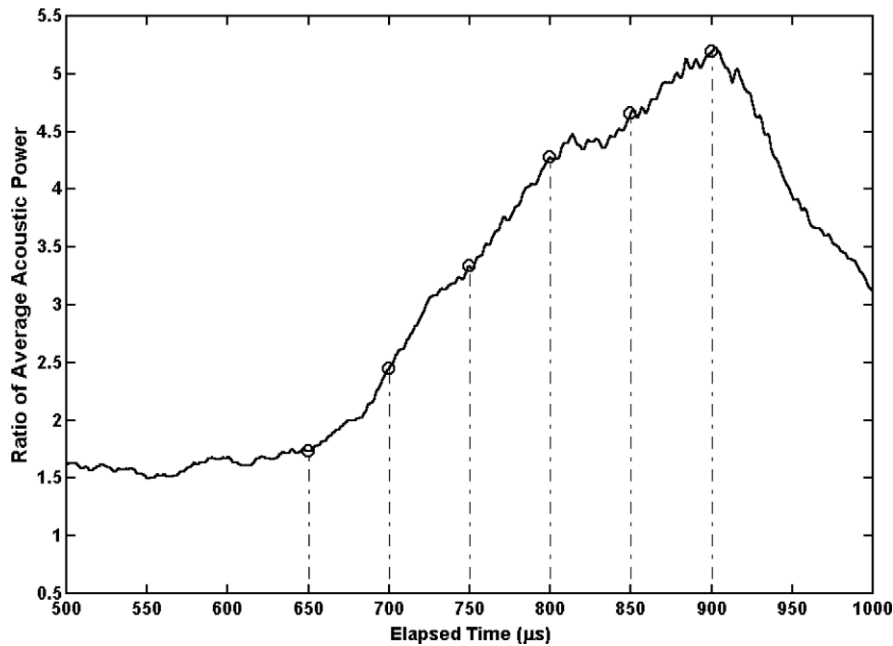


Fig. 9. The ratio of the average acoustic power transmitted through the rough interface to that transmitted through the smooth interface as a function of time (based on the spatial integration of the data in Fig. 8 and for data corresponding to different elapsed times t_c).

targets using a variety of processing methods. To reduce the number of variables in this comparison, these tests will use an angle of incidence of $33^\circ \pm 2^\circ$ upon a ‘smooth’ interface. The test protocols will be described in Section 3, and the results will be presented in Section 4.

3. Acquisition and processing

3.1. Control and data acquisition

The results shown so far represent measurements made to characterise the beam, in free field (Fig. 5) and in the sediment (Figs. 7 and 8). However in order to undertake target detection in the sediment, a different experimental arrangement was required [26]. To take sufficient numbers of measurements, an automated position control rig was mounted above the laboratory tank (Fig. 10), comprising a rectangular frame with two independent sliding beams. A sliding stage was attached to each beam, below which the acoustic reflectors were suspended. All the components of the rig near to the water were made from anodised aluminium and stainless steel to minimise corrosion. A stepper-motor and gearbox assembly was attached to each of the four sliding elements, allowing the reflectors to be positioned anywhere in the two-dimensional plane above the sediment. The centres of mass of each of the buoyant reflectors were centrally positioned to distribute evenly the stresses within the frame. The height and orientation of the reflectors were fixed so that they always remained pointing in the same direction. Slack in the gearbox resulted in a small error of up to ± 1 cm about the programmed position. The error in the mean position of the sliding elements was measured to be less than 1 cm over a travel length of 150 cm.

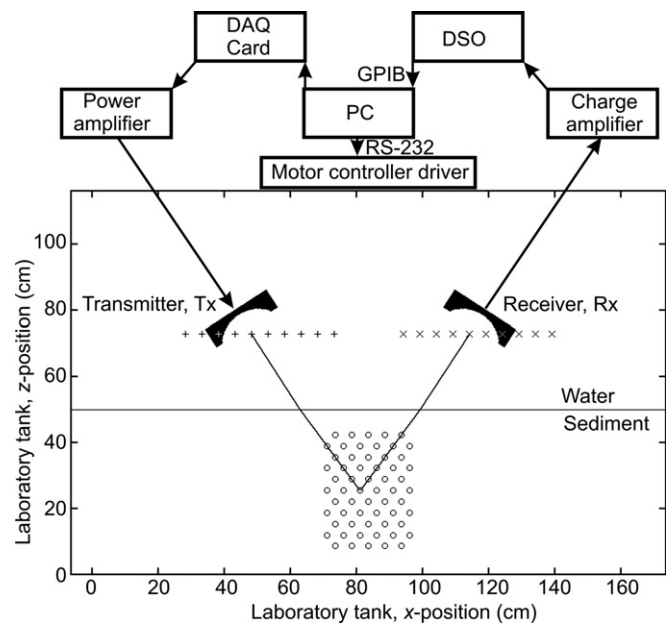


Fig. 10. The arrangement of the signal generation/data acquisition hardware that was used in the laboratory tank automated control system for the target detection tests of Section 4. Also shown is an example scanning pattern for the automated position control system, as viewed from the side of the laboratory tank. Symbols: + = discrete positions of the acoustic projector; x = discrete positions of the acoustic receiver; o = points of intersection within the sediment.

A dedicated computer, host to four stepper-motor control boards, and a separate power supply were used to drive the motors. Control commands were sent from a second, more powerful computer via an RS-232 null modem link.

The second computer was used to co-ordinate the entire signal generation/data acquisition process. It was equipped with a DAQ card that was used for both data acquisition and signal generation, and a GPIB card that enabled the remote control of a fast digital storage oscilloscope. The basic arrangement of the signal generation/data acquisition hardware is shown in Fig. 10.

Control software for the acquisition card, the oscilloscope and the stepper-motors was written using the Lab-View™ programming environment. A standard file format was adopted so that waveform data could be exported to other software packages, particularly Mat-Lab™, for post-processing and analysis.

Discrete positions were calculated for the acoustic transducers, such that the reflector beams intersected at a range of points in the middle of each xz -plane. For the target detection studies which will be described in Section 4, the arrangement followed the example shown in Fig. 10. Here the hydrophones are positioned 23 cm above the sediment surface, the reflectors are inclined such that the angle of incidence is $\theta_i = 33^\circ \pm 2^\circ$, and the angle of transmission θ_t into the sediment is $37^\circ \pm 2^\circ$ (as found through Fig. 7).

The symbols, + and \times in Fig. 10 correspond to the positions of the two hydrophones (acoustic projector and receiver, respectively). Acoustic beams projected into the sediment from these positions intersect at the 60 sample points marked by the symbols, \circ . These points cover an area 20 cm wide and 30 cm deep in the centre of the xz -plane. An example for one combination of source and receiver positions is indicated in the figure. By moving the transducers in the y -direction, i.e., out of the plane of the paper, it was possible to scan successive planes and, thereby, sample a three-dimensional volume within the sediment.

3.2. Options for signal processing

Figs. 12–16 will show measurements in which attempts are made to detect real objects, using a range of signal processing approaches to enhance contrast, and reduce the effect of noise, clutter and reverberation [68,69]. Each received waveform dataset is processed in two ways to compare their effectiveness when processing identical raw echo data: optimal filtering, and a synthetic aperture technique [68]. Particular characteristics of the target, such as resonances or directionality in the scatter, can be exploited.

Several candidate waveforms were possible for the outgoing pulse. These include modulation methods (amplitude modulation (AM); frequency modulated continuous wave (FMCW); continuous wave (CW); and pulse expansion/compression methods). Of these, CW systems were deemed inappropriate as they would generate reverberation problems in the test tank. Although pulsed AM waveforms have been tested with these targets, the results are not relevant for the comparative tests reported in this paper [68]. The output waveform for this paper was chosen to be a linear-swept FM pulse (Fig. 11). In terms of pulse expansion/compression techniques, this is a good choice if a high power and wide bandwidth are required. It was designed in the time-domain and extended over the entire operational bandwidth of the transducers (sweeping upwards in frequency from 20 kHz to 150 kHz). A $1/10$ cosine-tapered window was used to prevent unacceptable distortion of the frequency spectrum which abrupt signal truncation might engender.

The aim of the signal processing was to produce a three-dimensional representation of the subsurface volume, and if required there are a range of techniques to reduce noise and clutter before more advanced signal processing opera-

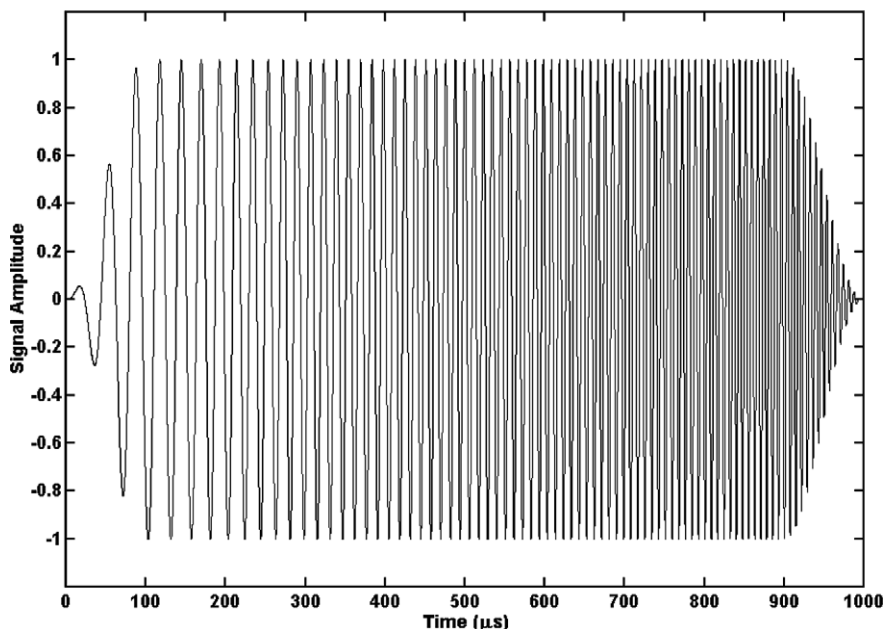


Fig. 11. The time windowed, linear-swept FM (chirp) pulse waveform with which the transmitter was driven.

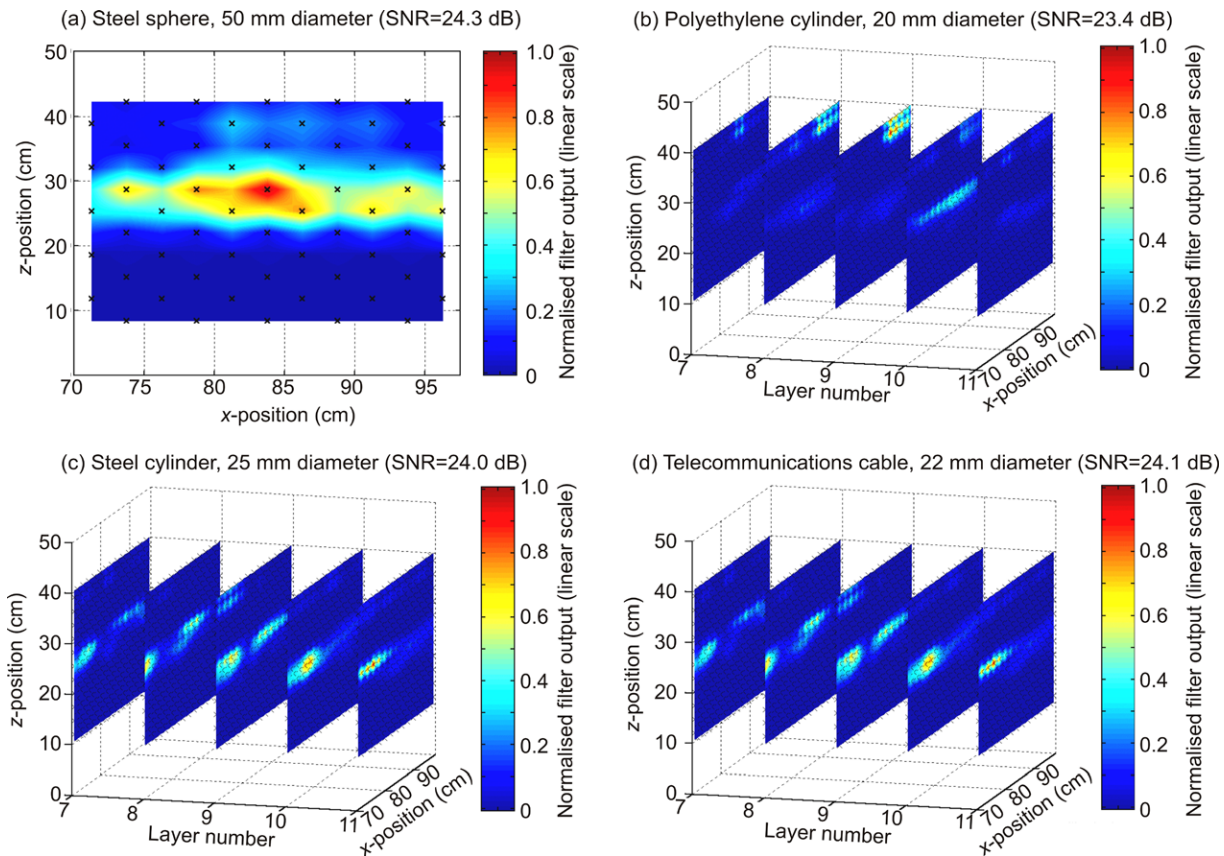


Fig. 12. The normalised, peak-squared, matched filter output (linear scale) from a target region containing (a) a steel sphere of 50 mm diameter (SNR = 24.3 dB), (b) a polyethylene cylinder of 20 mm diameter (SNR = 23.4 dB), (c) a steel cylinder of 25 mm diameter (SNR = 24.0 dB) and (d) a real lightweight telecommunication cable of diameter 22 mm (SNR = 24.1 dB). In Figs. 12–16, the z -co-ordinate is measured up from the base of the tank, such that the sediment/water interface is at $z \sim 50$ cm. In (b)–(d) of Figs. 12–16, the apparent background mesh in each plane is actually made up of small crosses \times indicating the measurement points.

tions are undertaken [68,70]. Two classes of advanced techniques were applied to enhance target detection [68]. First, waveform dependent methods can exploit a filter which, if it is assumed that an estimate of the incident waveform is available through a calibration experiment or modelling, can be designed to pick out the signal in the received waveform. Such a filter can modify the shape of the received signal, usually into a single peak, to increase the detection probability [68]. An obvious method of doing this is by Wiener filtering [71], where the desired output shape is used as an input to the filter design process. Second, target dependent methods can be used as a detection aid. These can exploit the distinctive scattering properties of some targets. In particular, regularly shaped objects (such as spheres and cylinders) have a set of resonances which impose a characteristic spectrum on the scattered signal when illuminated with broadband radiation. For example, the echoes generated from a smooth, solid, elastic cylinder insonified by a source of plane acoustic waves comprise diffracted waves, surface flexural waves and back-reflected compressional waves from within the target [68,72]. The scattered signal is dependent on the physical dimensions of the target and the mechanical prop-

erties of the material from which it is made. Modelling the scattering from the targets used in this investigation is discussed in Ref. [68].

3.3. Protocols for target detection experiments

The acoustic axes of the transducers were inclined at an angle of incidence of $33^\circ \pm 2^\circ$, and aligned such that they would intersect at discrete sample points within the sediment. Thus, each set of data comprised a series of pulse-echo measurements from a range of sample points.

Initially, each target was scanned with a sample spacing of 5 cm, giving 60 points in each of the five sample planes within the sediment, such that a total of 300 sample points were measured. If examination of the data for a given target indicated the possible (but not conclusive) presence of a target, a second scan was conducted with a reduced sample spacing, such that there were 300 points in each sample plane within the sediment.

The average waveform was obtained from 100 nominally identical scatters, thus reducing the level of the background noise signal by a factor of 10. Band-pass filtering in the 20–150 kHz range was performed to limit the system

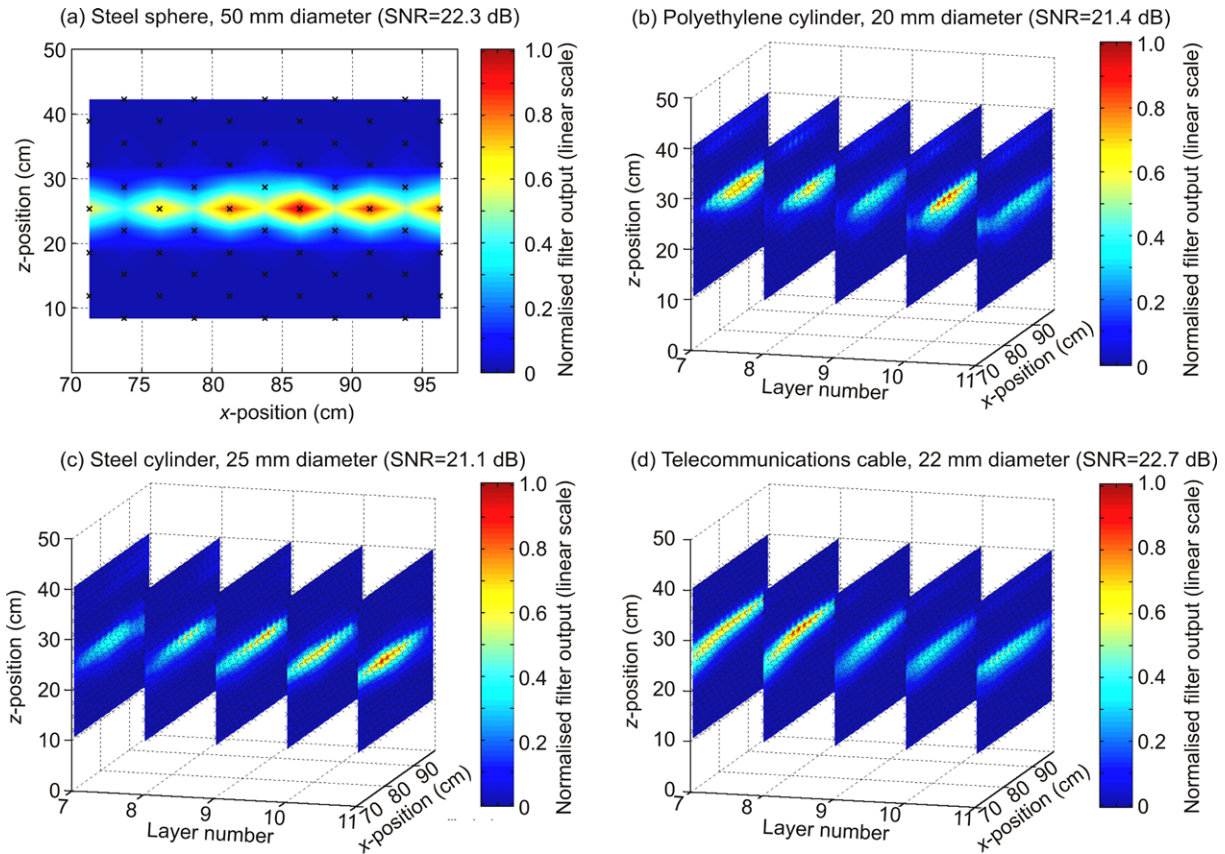


Fig. 13. The normalised, peak-squared, inverse filter output from a target region containing (a) a steel sphere of 50 mm diameter (SNR = 22.3 dB), (b) a polyethylene cylinder of 20 mm diameter (SNR = 21.4 dB), (c) a steel cylinder of 25 mm diameter (SNR = 21.1 dB) and (d) a real lightweight telecommunication cable of diameter 22 mm (SNR = 22.7 dB).

bandwidth to the maximum operational bandwidth of the transducers. Signal energy outside of this frequency range carried no useful information and could only have served to increase the noise level. The triggering level and pre-triggering delays of the acquisition system were used to align all the measured data within a common time frame. This was necessary to enable subsequent time windowing operations.

Subsequent to the pre-processing described above, the signal was processed in different ways, depending on whether target detection exploited optimal filtering (Section 3.3.1) or the synthetic aperture paradigm (Section 3.3.2). Processing details are given in Ref. [68]. In each case the output of the filter was squared and time windowed in a 50 μ s window (the duration being estimated from the known positional errors [68]).

3.3.1. Protocol for detection using optimal filtering

An optimal filter is one that is designed to select and modify the shape of a signal to increase the likelihood of detection of any targets that may be present. For measurements containing high levels of noise, such as those obtained in the field, this can be very useful [68,71]. A sample of the noise spectrum is usually required and can be obtained from separate measurements.

One approach to constructing an optimal filter that enhances performance is based on the Weiner, or inverse, filter. This represents the optimal linear filter that reduces the effect of the noise on a signal, using a minimum squared error principle. Details can be found in Ref. [68].

Alternatively one can employ a matched filter, which constitutes the optimum linear processor for increasing the SNR, when the corrupting noise is White and Gaussian [73]. The precise formulation employed in this study, can be found in Ref. [68]. A matched filter transforms the raw data at the receiver into a form that is suitable for performing optimum detection decisions, i.e., target/no target decisions.

Having determined the optimal filter for an arbitrary waveform (see [68]), it is necessary to find the waveform that best suits the application. In principle, the optimal filter concept can be applied to any waveform. However, certain waveforms give rise to less ambiguous measurements. In this application, high resolution and accuracy are required, i.e., the waveform should leave the least amount of ambiguity to contend with after the filtering process. Ref. [68] outlines how the construction of the ambiguity function can be used to quantify how well a particular waveform performs, and the resulting choice of a linear-swept FM pulse (Fig. 11).

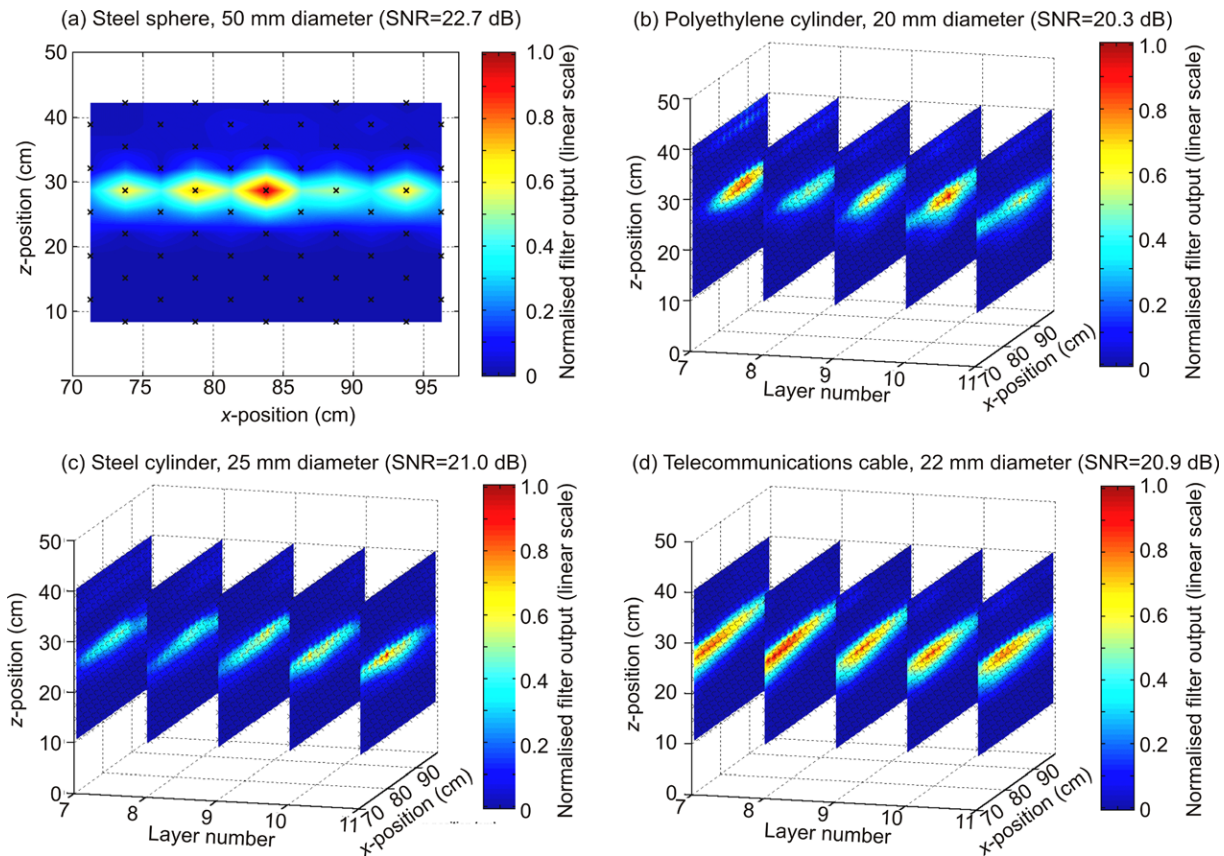


Fig. 14. The normalised, peak-squared, elastic-response-optimised, inverse filter output from a target region containing (a) a steel sphere of 50 mm diameter (SNR = 22.7 dB), (b) a polyethylene cylinder of 20 mm diameter (SNR = 20.3 dB), (c) a steel cylinder of 25 mm diameter (SNR = 21.0 dB) and (d) a real lightweight telecommunication cable of diameter 22 mm (SNR = 20.9 dB).

Both matched and inverse filters were used in this investigation [68]. They were adjusted to include the path-length-dependent attenuation measured in the sediment (see Section 2.2) and the frequency response of the measurement system. The scattering responses of the targets (i.e., both the resonant and rigid scattering responses of spheres and cylinders) were also included in the filter functions, making this a target dependent processing method [68,74]. After optimal filtering, the output signals were squared and time-windowed as described above. The peak value in the time window was recorded as the detection result.

3.3.2. Protocol for detection using the synthetic aperture paradigm

One method of increasing the signal level is to use an array of acoustic sources and receivers. In the implementation of this here, the transducers of the array do not coexist, but are generated through the relocation of a subset of transducers and combining the measurements taken at the various locations, a technique known as synthetic aperture sonar (SAS) [5,10,13,75]. An image is formed from a coherent sum of the pings that comprise the ‘aperture’, after they have been compensated for the appropriate propagation delays associated with each the source/receiver location.

The experimental conditions are well-suited to the requirements and limitations of SAS, as the distance from the detection platform to the target is only a few metres, and the platform speed is slow. Although physically the rig is stable and the water almost motionless, the roughness on the sediment/water interface may introduce an effective instability which degrades the performance of SAS [68].

4. Results

The range of detection techniques discussed in Sections 3.2 and 3.3 were tested with four different single targets: a steel sphere, 50 mm in diameter; a polyethylene cylinder, 20 mm in diameter; a steel cylinder, 25 mm in diameter; and a section of real, lightweight telecommunication cable, 22 mm in diameter. The cylinders (all 50 cm long) were oriented so that their long-axes were perpendicular to the sample planes, i.e., each plane sliced through a cross-section of a cylinder. One at a time, these targets were buried at depths of 20–30 cm below the sediment/water interface, near the middle of the tank. The locations of the ‘sample’ points (marked by the symbol \times in the figures) are discussed below: they correspond to the centre of the sensing volume (Section 2.3), and the variation of beam pattern between neighbouring sensing points can be estimated for a given

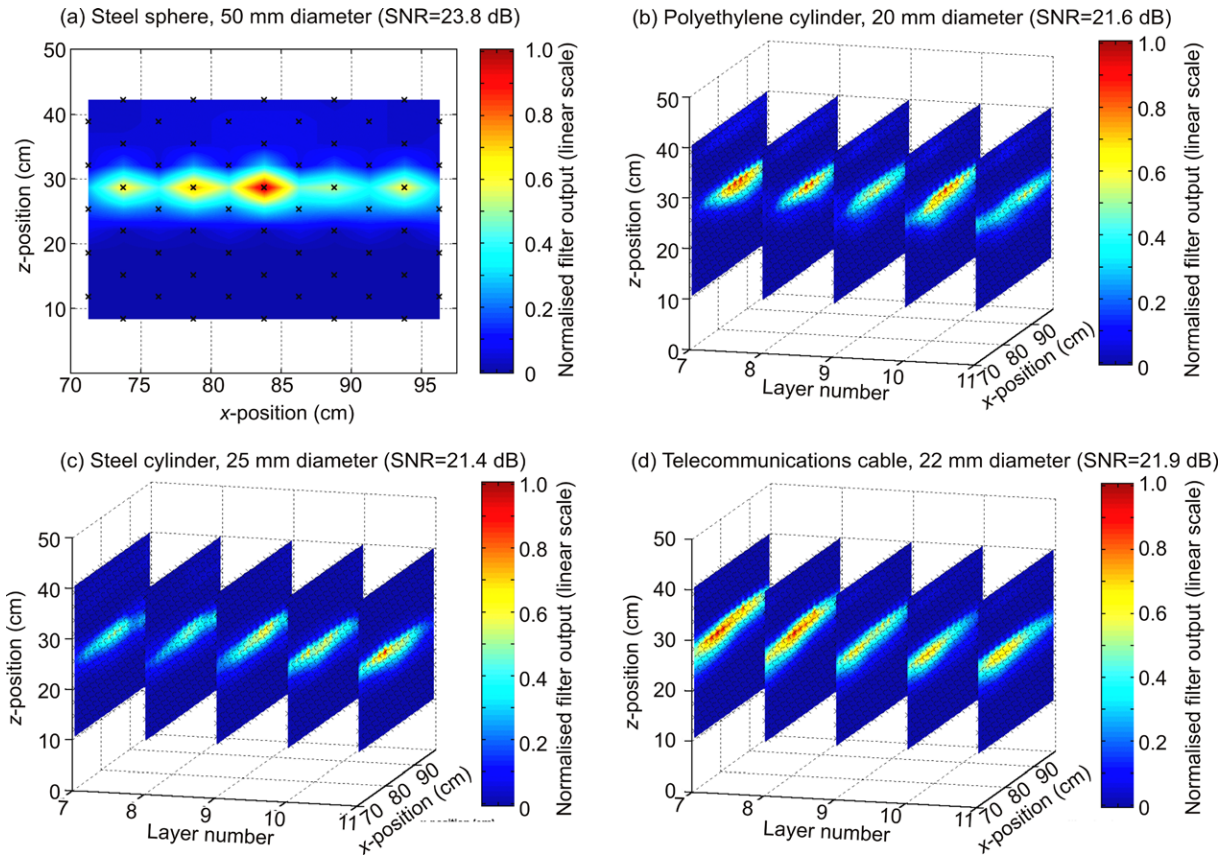


Fig. 15. The normalised, peak-squared, rigid-response-optimised, inverse filter output from a target region containing (a) a steel sphere of 50 mm diameter (SNR = 23.8 dB), (b) a polyethylene cylinder of 20 mm diameter (SNR = 21.6 dB), (c) a steel cylinder of 25 mm diameter (SNR = 21.4 dB) and (d) a real lightweight telecommunication cable of diameter 22 mm (SNR = 21.9 dB).

scan using Fig. 7. Note from Section 3.1 that there is a ± 1 cm uncertainty in the positioning system.

With reference to the experimental arrangement described in Sections 3.1 and 3.3.1, a sample spacing of 5 cm was used for measurements involving the steel sphere, and a spacing of approximately 2 cm was used for the cylindrical targets. That is to say, the scanning pattern of 60 sample points was used for the sphere, and the pattern of 300 sample points for the cylinders (detailed below).

In each image, the z -direction corresponds to vertical position in the sediment, measured upwards from the bottom of the laboratory tank, and the x -direction corresponds to horizontal position. In the case of the buried cylindrical targets, the x -direction is perpendicular to their long-axes.

The sample points are marked in each image (Figs. 12–16) using the symbol, \times . For the buried sphere, 60 sample points were measured in each of the five vertical planes within the sediment. The processed results were then spatially averaged. For the cylindrical targets, 300 sample points were measured in each of the vertical planes. The processed results are shown without any spatial averaging having been performed. Continuous images were formed by interpolating between each sample point using a piecewise bilinear interpolation algorithm.

The signal-to-noise ratio (SNR) was chosen as the figure-of-merit that would allow comparison between alternative processing techniques. It was calculated for each set of measurements by dividing the peak-squared value at the filter output (with no normalisation having been applied) by an estimate of the average noise level. The average noise level was determined by applying similar processing to a set of baseline measurements, which were obtained when the experiment tank contained no buried targets, and calculating the mean-squared value at the filter output. The SNR values that were obtained are noted alongside each of the graphs in Figs. 12–16.

4.1. Result for detection using the optimal filtering

The peak-squared optimal filter output was calculated from every sample point for each different buried object. The results are presented in Figs. 12–15.

The signal-to-noise ratio was calculated so that a comparison could be performed between the different sets of results. It was calculated using a similar method to that described in Section 3.3.1. That is to say, the SNR for each set of measurements was found by dividing the peak value by an estimate of the rms noise level. (Values of SNR in decibels are noted on each of the graphs).

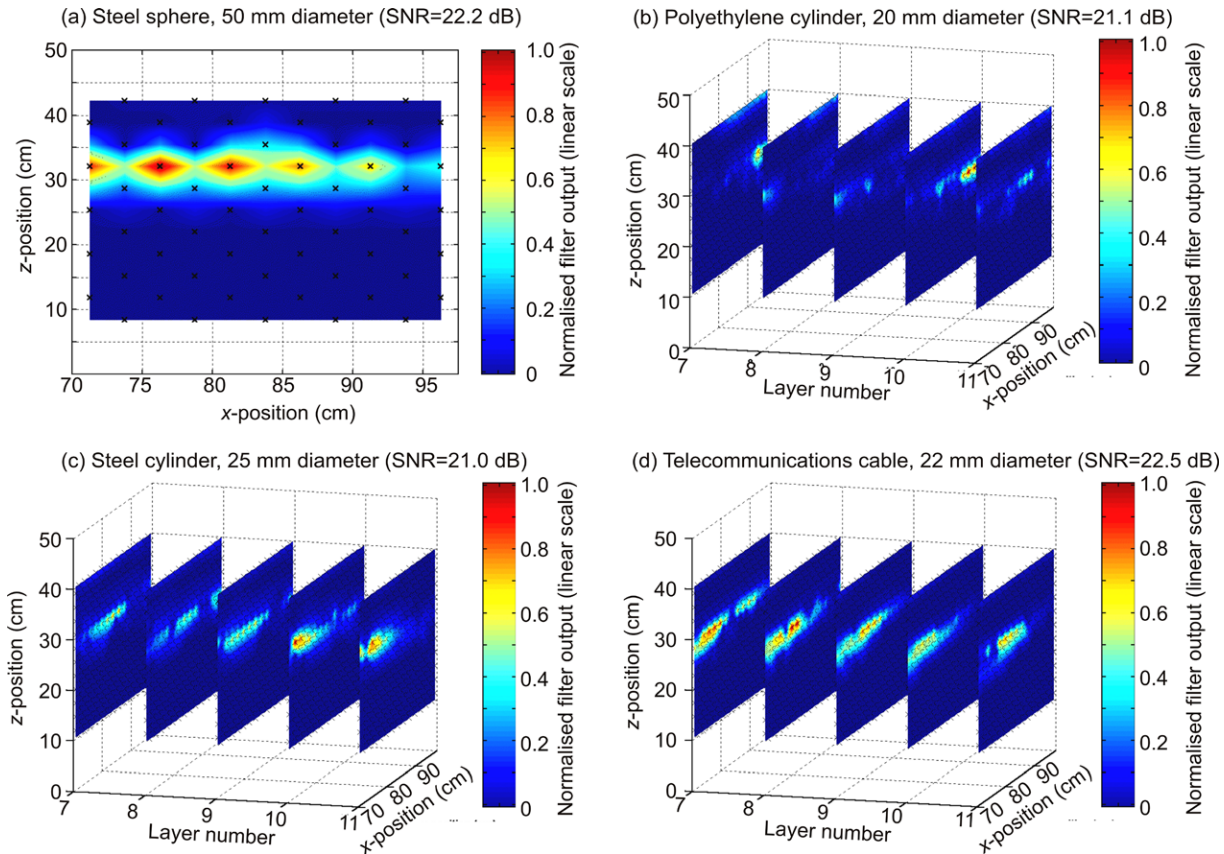


Fig. 16. The synthetic-aperture-enhanced, inverse filter output from a target region containing (a) a steel sphere of 50 mm diameter (SNR = 22.2 dB), (b) a polyethylene cylinder of 20 mm diameter (SNR = 21.1 dB), (c) a steel cylinder of 25 mm diameter (SNR = 21.0 dB) and (d) a real lightweight telecommunication cable of diameter 22 mm (SNR = 22.5 dB).

The average¹ signal-to-noise ratio for the matched filter (Fig. 12) measurements is in the range 23.6–24.3 dB (Table 1). However, the peak signal levels in some of the results (such as Fig. 12b, the polyethylene cylinder) correspond to clutter rather than to the target. Therefore, the SNR values obtained from these measurements must be treated with some caution when being compared with other results.

The average SNR for the inverse filter measurements (Fig. 13) is less than for the matched filter, having a value in the range 21.1–22.6 dB (Table 1). However, there is a marked reduction in the level of clutter in the output plots and, significantly, a higher proportion of the sample points in the target region indicate the presence of a buried object than was the case for the matched filter. Therefore, the inverse filter is judged to be better suited to the detection of buried objects in a cluttered environment.

¹ In this paper, the quoted ‘averages’ of series of decibel values were obtained as follows: Firstly, each decibel value was converted into a linear system of units. The average and the standard deviation of these values were then calculated, to give a range of values with an uncertainty of ± 1 standard deviation centred on the mean. Finally, this linear result was converted back into the logarithmic (decibel) system of units, to give a range of values that encompassed an estimate of uncertainty.

For the inverse filter, optimised to the elastic scattering response of the targets (Fig. 14), the average SNR is in the range 20.0–22.3 dB (Table 1). This overlaps the average SNR of the basic inverse filter (Fig. 13). Therefore, these results do not show any quantitative improvement in the use of this filter instead of the basic inverse filter. However, the filter output in the region of the buried targets is, qualitatively, more distinct than in the previous case.

For the inverse filter, optimised to the rigid scattering response of the targets (Fig. 15), the average SNR value is in the range 20.9–23.4 dB (Table 1). As in the elastic-scattering-optimised case, this overlaps the average SNR of the basic inverse filter (Fig. 13). That is to say, neither of the optimised filters show a quantitative improvement in SNR. However, the target localisation is better than that obtained using the basic inverse filter in both cases.

4.2. Result for detection using the synthetic aperture paradigm

The data presented in Section 4.1 were reprocessed following the synthetic aperture paradigm. For each sample point, a synthetic aperture was formed from the recorded signals corresponding to the point itself and to the nearest four surrounding points. The signals were phase-adjusted

Table 1

The signal-to-noise ratios (expressed in dB) that have been calculated for each detection process and target type

Detection process	Steel sphere	Polyethylene cylinder	Steel cylinder	Real cable	Average SNR (see footnote 1)
Matched filter	24.3	23.4*	24.0	24.1	23.6–24.3
Inverse filter	22.3	21.4	21.1	22.7	21.1–22.6
Elastic-response-optimised inverse filter	22.7	20.3	21.0	20.9	20.0–22.3
Rigid-response-optimised inverse filter	23.8	21.6	21.4	21.9	20.9–23.4
Synthetic-aperture-enhanced inverse filter	22.2	21.1	21.0	22.5	20.9–22.4

An asterisk indicates that the peak signal corresponds clutter rather than to the target.

to match the signal corresponding to the central point, using the time-of-flight equation (Eq. (14) of Ref. [68]). Then the average value over the five points was calculated. The resulting signal was processed using the basic inverse filter and a time window was applied to the filter output (according to the method described in Section 3.3). The results are shown in Fig. 16.

In the synthetic aperture case (Fig. 16), the average² SNR is 20.9–22.4 dB (Table 1). When compared with the basic inverse filter, which exhibited an average SNR of 21.1–22.6 dB (Fig. 13), the synthetic-aperture-enhanced filter does not seem to yield any improvement in performance. Moreover, it should be noted that the high signal regions in Fig. 16 are not as well localised as before. The apparent lack of improvement using the enhanced technique may be attributed to the fact that only a small number of points were used to create the synthesised aperture. Further investigation using a larger synthetic aperture is required before any conclusions may be drawn as to whether this technique offers any significant improvement.

5. Discussion

5.1. Comparison of techniques for target detection

A comparison of the buried object detection techniques presented in the previous sections is given below. For each technique and buried target type, the signal-to-noise ratio at the output of the processor was recorded. These are summarised in Table 1. It should be noted that in some cases, where the peak clutter levels were comparable to the peak target signals, the SNR estimate may actually be more representative of the peak clutter-to-noise ratio. The measurements for which this was the case have been marked in the table by an asterisk.

The matched filtering results contained significant clutter (contributing to the SNRs observed) and target localisation was unremarkable. Inverse filtering resulted in lower SNRs than the matched filter, but from the output plots it is clear that the clutter level was significantly reduced and target localisation greatly improved.

Target optimisation resulted in better localisation of the buried objects in the output images. However, this was not

accompanied by an increase in the overall SNR. Given that the resonant scattering response in sediments was not expected to be the same as the theoretical response (for which it was assumed that the surrounding medium was a fluid), it is not entirely surprising that this was the case.

For the rigid scattering inverse filter with synthesised aperture enhancement, the average SNR is in the range 20.9–22.4 dB. This level is similar to the average SNR for the basic inverse filter, which was found to be in the range 21.1–22.6 dB. However, localisation in the target regions was found to be poor. This is symptomatic of the synthesised aperture process which requires the returned signals to be aligned to within a fraction of a wavelength (typically less than 1/5 of a wavelength). It was concluded that further investigation into the use of this technique is required.

Although not presented in detail here (since the environment that is of interest in this study is highly cluttered) matched filter measurements optimised to resonant and rigid targets have shown similar results to the inverse filter case. It is surmised that the matched filter would be a better choice than the inverse filter for use in a noisy environment, this being consistent with the filter behaviour predicted in Section 3.3.2.

6. Summary

The difficulties associated with the detection of targets generally increase as the acoustic impedance mismatch between the target and the host medium decreases [68]. This paper addresses the issue of the detection of polyethylene, fibre optic, and steel targets which are buried in saturated sediment. For data from a bistatic sonar system in a test tank, two main approaches to the detection problem were described, based on waveform dependent filtering using FM pulse compression waveforms. The techniques should be generally applicable to monostatic, bistatic and multistatic sonar systems mounted on, for example, an ROV.

Overall, the algorithms presented in this paper (and the acoustic detection system in general) have proven to be very successful in detecting objects buried at depths of between 25 and 30 cm in the sediment.

In every case, either 60 or 300 sample points were measured over a series of planes extending vertically into the sediment. It was found that with 60 points (having a sample spacing of 5 cm) the resolution was not high enough to

² Refer to footnote 1.

provide conclusive detection results. Conversely, with 300 points (having a sample spacing of around 2 cm) the buried objects could be detected easily. In a practical system, where the time available for scanning a volume of the seabed may be quite limited, this issue needs to be addressed. The sample spacing may be adjusted to find the lowest resolution that still provides acceptable performance, although of course an appropriate budget would allow the deployment of rapid beamsteering solutions to replace the low-cost mechanical system deployed in this paper.

Simple matched filtering was shown to be useful in an environment dominated by noise. However, the optimal filter was shown to be more successful in dealing with the cluttered seabed environment. This is particularly important in light of Section 2.5.2, since surface roughness could give rise to an increase in clutter at the receiver.

Target optimisation techniques had mixed success. When the target scattering responses (for both rigid and the elastic scattering) were incorporated into the filters, qualitative improvements in target localisation were observed. However, these were not accompanied by an increase in the average values of the signal-to-noise ratio.

Synthetic aperture techniques have also been investigated. It was suggested that these may have the potential to improve the performance of a detection system. However, the positional error in the laboratory apparatus and the small number of measurement positions used to form the synthetic aperture meant that no significant performance improvement was actually observed.

The Appendix describes a possible technique for the detection of one class of ‘difficult’ targets, specifically the next generation of optical fibre telecommunications cables which may lack the metallised cores of current commercial submarine fibre optic communications cables, and which allow them to be detected using magnetometers [20,76].

Acknowledgements

TGL is grateful to the Engineering and Physical Sciences Research Council and Cable and Wireless for providing a studentship for RCPE to conduct this project, and to DC Finfer for assistance in the production of greyscale versions of the colour figures. The authors are grateful to Cable and Wireless for loan of the OTDR.

Appendix. Acousto-optical options for the particular case of optical fibres

1. Background

The methods considered so far in this paper have investigated sonar techniques (specifically the bistatic option, although adaptation to the monostatic case would be simple) for the detection of targets in general when they are buried in saturated sediment. There are the additional possibilities for one specific type of target: the optic fibre [77]. For example, an external acoustic field might be directed at

the cable in order to change its properties (notably, its optical transmission properties) to facilitate its detection by some other means. In this way, for example, it should be possible to determine the position of the cable by using established optical techniques to detect when the footprint of the acoustic beam passes over it.

The detection protocol associated with this technique is summarised in Fig. 17. Here the acoustic field is projected by a surface vessel, although an ROV (remotely-operated vehicle) could equally be used. Three cables are shown in the example. If the requirement is for cable B to be found, then the acousto-optic detection system should be connected to its input. The position of the cable is determined using the fact that it will be directly beneath the footprint of the acoustic beam at the time at which a change in the optical transmission properties of the fibres is detected. An advantage of this system is that even if the beam passes over cables A and C there can be no danger of confusing them with the broken cable, since the detection system is connected directly to cable B.

It should be noted that it is not the cable that is being detected using this approach. Instead the influence of the acoustic source is detected by the fibre within the cable, which acts as a sensor. The advantage of this method is that the issues surrounding scattering at the water–sediment interface, and back-scattering from the target, become largely irrelevant. Simply by directing an acoustic beam of sufficiently high acoustic intensity at the seabed, it should be possible to locate the target. The specifics of the cable technology would have to be included in an assessment of the practicability of any eventual system, but this is not addressed in this paper because its purpose is to outline techniques which may be applicable to future cable types (for example, whilst repeaters in submarine cables [20,77] would discard the acoustic modulation of the optical signal during the conversion into an electrical

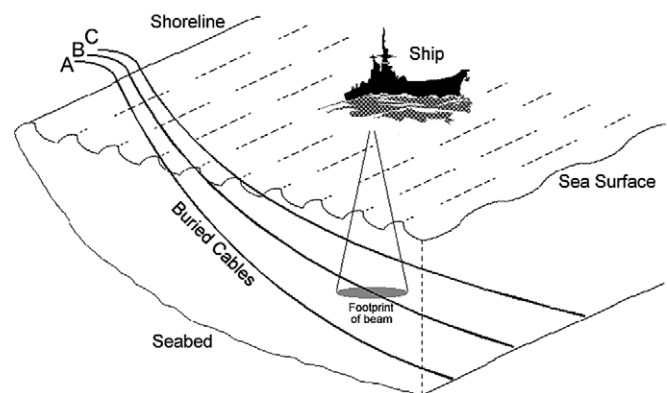


Fig. 17. The detection protocol associated with an acousto-optic detection system. In this scenario, an acoustic beam is projected from a surface vessel (though it could also be projected from an ROV). As the footprint of the beam passes over cable B, its effect on the optical transmission properties of the inner fibres may be detected using a land-based system. By comparing the position of the footprint over time with the time of detection, it should be possible to determine the location of the cable.

signal, unrepeatable systems based on the erbium-doped fibre amplifier do not need to convert optical signals into electrical signals for amplification). The potential for this technique was investigated using an optical time domain reflectometer (OTDR).

2. The OTDR experiment

The OTDR launches a short pulse of laser light into a fibre under test. As the pulse propagates through the fibre, loss occurs because of Rayleigh scattering from random, microscopic variations in the refractive index of the fibre core (other loss mechanisms will be discussed in Section 3). A fraction of the light is scattered back towards the detector. The processing electronics measures the level of back-scattered light as a function of time relative to the input pulse (Fig. 18).

If the fibre is homogeneous and subject to a uniform environment, the intensity of the back-scattered light decays exponentially with time because of the intrinsic loss in the fibre. However changes in the optical properties of the fibre, such as might occur in the presence of an applied acoustic field, generate regions in the fibre of differing attenuation (Fig. 19). Reducing the duration of the pulses increases the spatial resolution, but decreases the maximum sensing range because of the reduced signal energy. For a discussion of the practical considerations associated with OTDR (including the limitations on the system resulting from chromatic dispersion, contaminants in the glass, dispersion, and the differing responses of the fibre to micro-bends and to clean and partial fractures), see Ref. [77].

The particular OTDR device that was used (an Anritsu MW9070A OTDR) exhibited an optical bandwidth of around 60 nm [78]. That is to say, at an optical wavelength

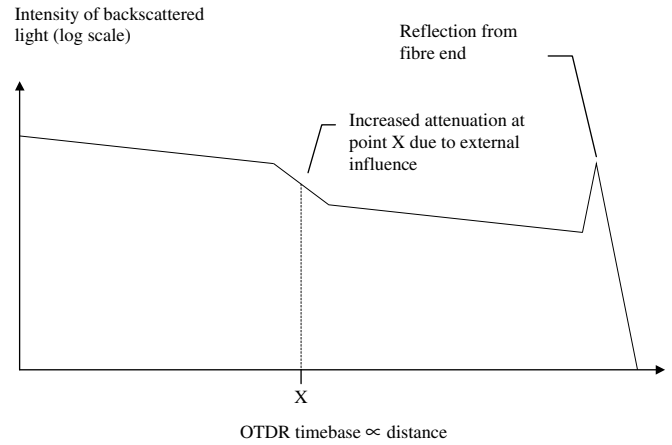


Fig. 19. Schematic of an OTDR output trace. The intensity of the back-scattered signal is displayed as a function of time (proportional to fibre length). An almost constant attenuation is observed over the length of the fibre except at point X where some external influence has caused the attenuation to increase.

of 1550 nm the optical bandwidth of the OTDR would have been around 5 THz. This is much greater than the Brillouin frequency shift in silica which is ± 11 GHz. Therefore, it should be noted that this device was not capable of isolating Brillouin back-scattered signals from the back-scattered Rayleigh signal since its output would have encompassed all the back-scattered signals that existed within the optical bandwidth.

The apparatus is depicted in Fig. 20. The OTDR was connected to a 1.8 km length of monomode optic fibre. The refractive index was refractive index of 1.466, and the other properties of this fibre were similar to those shown in Table 2. The outer jacket was made of acrylic and the overall diameter was around 1 mm. The end of the fibre was clipped to give a strong reflection, which was easy to identify in the OTDR back-scatter trace. The acoustic source was purpose-built using a piezoceramic hollow tube transducer (PZT-4 Lead Zirconate Titanide,

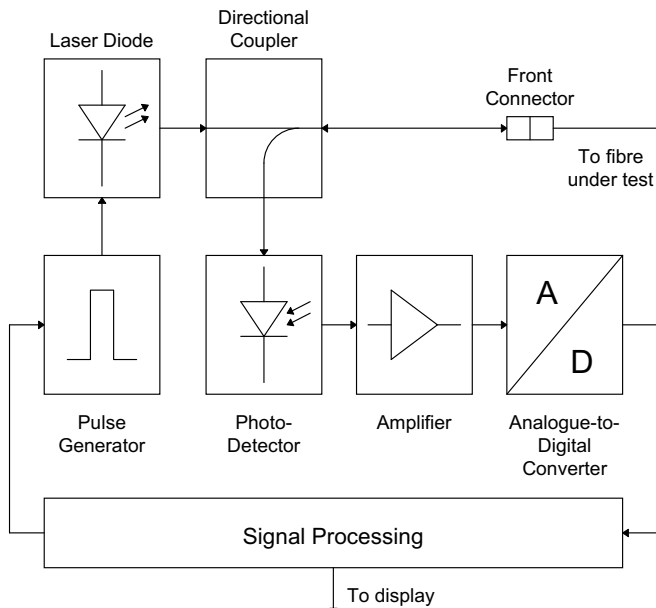


Fig. 18. The architecture of an optical time-domain reflectometry system.

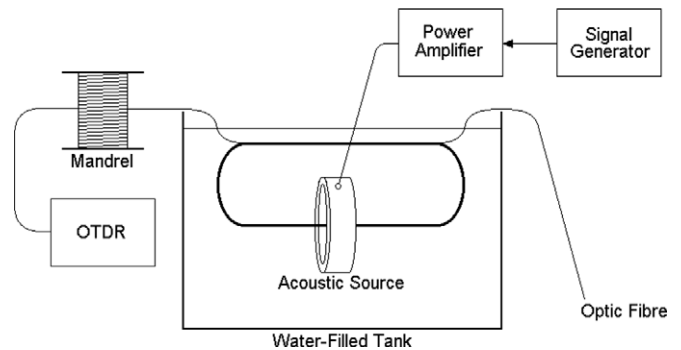


Fig. 20. The apparatus used in the OTDR experiment. The OTDR was connected to a 1.8 km length of optic fibre wound on a mandrel. The final 8 m of fibre was wound through a submerged tubular acoustic source. The fibre was excited using the acoustic source, and the back-scattered optical signal was measured using the OTDR.

Table 2
The composition, dimensions and elastic and elasto-optic coefficients of a typical single mode optic fibre

Fibre parameter	Core	Layer 1	Layer 2	Layer 3
Composition	SiO ₂ GeO ₂ (trace)	SiO ₂ (95%) B ₂ O ₃ (5%)	SiO ₂	Silicone
Radius (μm)	2	13	42	125
Young's modulus (GPa)	72	65	72	0.0035
Poisson's ratio	0.17	0.149	0.17	0.49947
p_{EM11}	0.126	–	–	–
p_{EM12}	0.27	–	–	–
Refractive index	1.458	–	–	–

See Ref. [77] for details.

with 104 mm inner diameter and a 6 mm wall thickness [79,80], encapsulated in a light-duty epoxy resin.

The final 8 m of fibre was wound 10 times through the hollow centre of the tube transducer, with the final metre left to hang freely. Eight frequencies were identified at which the acoustic source was found to be capable of producing an on-axis sound pressure level of 210 dB re 1 μPa. At a wavelength of 1550 nm, the shortest duration optical pulses that the OTDR could generate were 20 ns. This duration corresponded to a pulse length of 4 m in the fibre. The output trace was adjusted to measure the back-scattered optical power in a 4 m length of fibre ending 1 m before the reflective end.

This meant that, at the start of the OTDR measurement, the leading edge of the optical pulse would have reached the middle of the length of fibre wound through the acoustic source. The trailing edge of the pulse would have just entered this region of the fibre. Similarly, at the cessation of the OTDR measurement, the leading edge of the pulse would have reached the end of the wound length of the fibre. The trailing edge would have reached the middle of this region of the fibre. Hence, throughout the 4 m OTDR measurement window, the optical pulse would have resided

entirely within the region of fibre that could have been excited by the acoustic source.

An example of the OTDR output trace is shown in Fig. 21. In the case shown the fibre was not excited by the acoustic source. The back-scattered power in the measurement region (between the two cursors) reduces at a significantly greater rate than in the fibre before this region. The increase in loss is due to the radiation of optical power from the bends in the section of fibre wound through the tube transducer.

The back-scattered optical signal was measured with no acoustic excitation and with a 210 dB re 1 μPa excitation at each of the output frequencies. In order to be certain of a statistically significant result, 1000 averages of the signal were performed in each case. The measurements were then repeated to check that they were consistent.

Under the influence of an acoustic field, the back-scattered optical power was observed to increase over the OTDR measurement window. Changes in back-scatter as a function of acoustic frequency for the two sets of measurements are presented in Fig. 22. In this instance, 'change' is defined as being the difference, in decibels, between the measurements with and without acoustic excitation. In other words, the figure shows the back-scattered optical power measured in decibels relative to the back-scattered optical power with no acoustic excitation.

It was expected that the coupling between the fibre and the acoustic field would improve as the acoustic wavelength decreased, implying that the back-scattered optical power should increase with frequency. This is consistent with the change that was observed. That is to say, the data points in Fig. 22 tend, asymptotically, towards a maximum value at high frequencies, and follow the expected sigmoid model [77].

These results indicate that acoustically generated stresses can cause a change in the back-scattered optical power, as measured using a conventional OTDR. However, the observed change was found to be very small (i.e., the change in optical power was around 0.5 dB for a sound pressure level of 210 dB re 1 μPa).

Therefore, it has been concluded that for a cable detection system of this kind to be successful, a specially designed OTDR would be required, such as an OTDR which exploits a sensitive interferometric system designed to measure changes in phase. Another alternative would

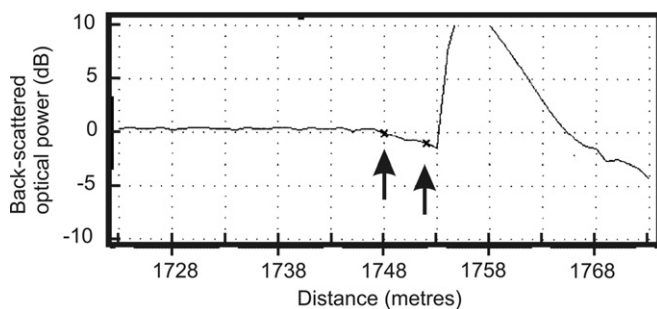


Fig. 21. An example of the OTDR output trace with no acoustic excitation. With a 1550 nm optical wavelength, 20 ns pulse width and refractive index of 1.466, the back-scattered optical power is displayed as a function of distance. The decrease in the region between the two cursors (arrowed at distances of 1748 m and 1752 m) was caused by radiation at bends in the fibre. The distinct reflection from the end of the fibre can be seen one metre beyond this region. (Note that the end-reflection has been clipped for display purposes only in order to allow the region between the two cursors to be visible in the figure: no clipped data were used for processing).

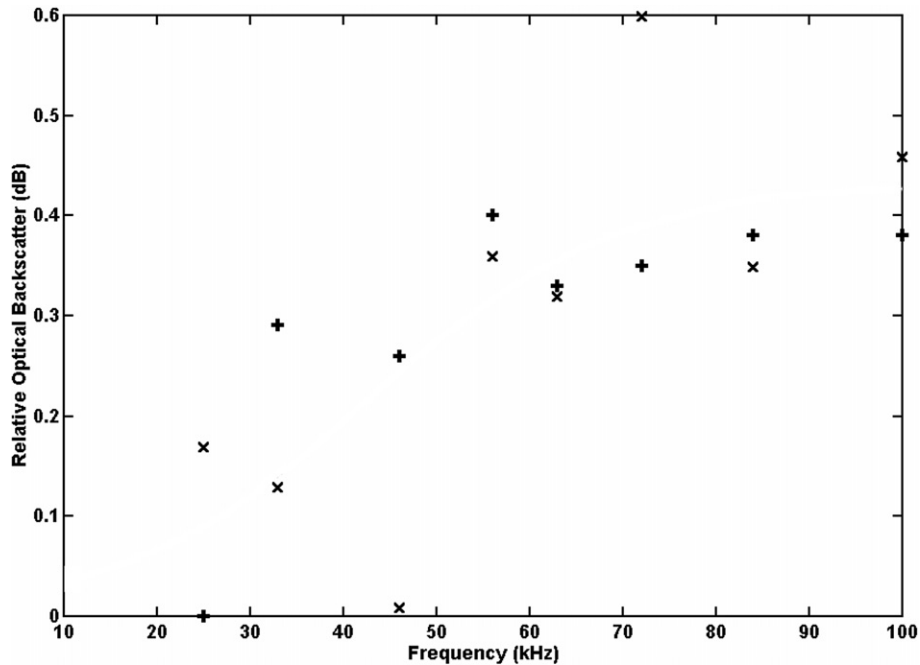


Fig. 22. Two sets of data (+, ×) showing back-scattered optical power in decibels as a function of the acoustic excitation frequency. The values were calculated relative to the back-scattered optical power in the case when there was no acoustic excitation.

be an OTDR which exploits one of the non-linear processes that can occur in optical fibres, which impart a frequency shift to the scattered light. The potential for such techniques to detect buried marine optic fibre telecommunications cables is discussed in the next section, and detailed in Ref. [77].

3. Non-linear optical process in fibres

There are four important processes to consider in non-linear processes in monomode, optic fibre transmission systems: Raman scattering; Brillouin scattering; self-phase modulation; and parametric, four-photon mixing [77,81]. These can lead to signal loss, pulse spreading, cross-talk and even physical damage to the optic fibre. The Raman and Brillouin scattering processes give rise to a difference in frequency between the incident light and the scattered light. Components which lose energy in the scattering process, and therefore have lower frequency, are referred to as Stokes components [77,82]. Those which gain energy and increase in frequency are referred to as anti-Stokes components.

The back-scattered signal in Raman scattering consists of light of the same frequency and weak, sideband components. The difference between these sidebands and the incident frequency is characteristic of the vibrational modes of molecules in the material. This is in general a greater frequency shift than is engendered by Brillouin scattering, which is the consequence of the interaction between light and thermally generated acoustic waves in the medium. The acoustic wave produces density variations which result in a periodic modulation of the material dielectric constant.

Scattered light is, effectively, Doppler-shifted by the acoustic wave.

For the laboratory experiment to be studied here, Brillouin scattering offers many advantages over the use of Raman scattering. Whilst optical wavelengths of 800–900 nm are popular for low-cost, short-haul systems, a better choice for telecommunication is the 1300 nm minimum dispersion wavelength. However, most modern long-distance systems use the narrow window around the 1550 nm minimum absorption wavelength. For a 1550 nm OTDR system, the wide bandwidth occupied by the Raman signal means that it occupies the region of strongest absorption in the frequency–attenuation curve. The Brillouin interaction, on the other hand, occupies a much narrower bandwidth and is closer in frequency to the Rayleigh signal. This means that it can make much better use of the minimum dispersion window. Whilst the greater frequency shift inherent in Raman scattering offers some advantages (e.g. with respect to cross-talk separation between the input pulse and any strong reflections [77]), in such circumstances the Raman signal is around 30 dB below the Rayleigh signal.

The principle of operation of the Brillouin optical fibre sensor is similar to that of the OTDR, the main difference being that the scatter mechanism is Brillouin instead of Rayleigh. Hence the term ‘Brillouin OTDR’ (BOTDR) is used [77,83].

At a temperature of 4 °C, the ratio of the power of the Rayleigh scatter, to that of the Brillouin scatter (the Landau–Placzek ratio) is 20.8, such that each of the two Brillouin components (Stokes and anti-Stokes) are approximately 16 dB below the Rayleigh signal [77]. The

radial sensitivity of a typical glass fibre is around 9 kHz/ μ strain. This corresponds to an applied stress, or pressure, sensitivity of approximately 130 Hz/kPa (given that the Young's modulus of glass is around 7×10^{10} Pa) [77]. Even with a sensitive interferometric system this modulation would be very hard to detect, given that the optical frequencies are in the terahertz band. Although in principle account should be taken of the effect of temperature changes on the optical frequency, in practice this effect is small (i.e. in the range 0–200 °C it is ~ 1 MHz/°C [77]).

The related acousto-optic effect not only exhibits a similar pressure sensitivity to that inherent in Brillouin scattering, but also takes into account the physical change in the length of the fibre, which may result in a much higher sensitivity. The most successful optic fibre hydrophones are those based on interferometry [77,84,85]. Such systems measure the change in relative phase between a light beam transmitted into a fibre and the same beam exiting the fibre. This phase change is caused by changes in physical length and refractive index which are directly related to changes in pressure. The total phase change is the sum of many small changes which are accumulated as the incident light is transmitted. However, in the current scenario (Fig. 17), access is only available to one end of the fibre. Therefore, to measure the change in phase, light must be returned from the far end. This is possible if the break in the fibre is reflective; light will be returned along the same path, experiencing twice the phase change. Evans and Leighton [77] showed that, in order to estimate the magnitude of this effect if applied to the scenario of Fig. 17, account must be taken of the anatomy of practical optic fibres, which comprise a glass core surrounded by layers, which are also

made of glass, with an outer jacket of plastic [20]. In a telecommunication cable several fibres are bundled together to form a single fibre unit which is, itself, sheathed in layers of insulation, armour, etc. However, an understanding of the physical processes at work can be obtained from a model of a single, multi-layered fibre [86,87]. Evans and Leighton [77] used in this model data from Cable & Wireless for a typical monomode fibre, for the core and three layers (Table 2).

A hydrostatic boundary condition was chosen, this being the most appropriate for a long fibre. An outer jacket, layer four, was included. The radius and Young's modulus of this layer was varied while the bulk modulus, K_b , was fixed at a value of 4 GPa. The set of pressure sensitivity curves that resulted from these calculations are shown in Fig. 23.

As the coating gets very thick the pressure sensitivity approaches a limit which is independent of the Young's moduli. This suggests that for very thick coatings the magnitude of the strains in the fibre are dependent on the bulk moduli alone. Fig. 24 confirms this to be the case. In this calculation the radius of the outer layer was fixed at 3 mm and Young's modulus set at 0.1 GPa. The curve is inversely proportional to the bulk modulus (i.e., linearly proportional to the compressibility) of the outer layer. At smaller radii the sensitivity relationship is more complicated, being a function of changes in both elastic moduli.

These results demonstrate that a greatly enhanced pressure sensitivity can be achieved using a clad, rather than an unclad, fibre [77,88]. This can be further improved by using a coating with a high compressibility, which is precisely the case for non-metallised fibre optic cables. It has been dem-

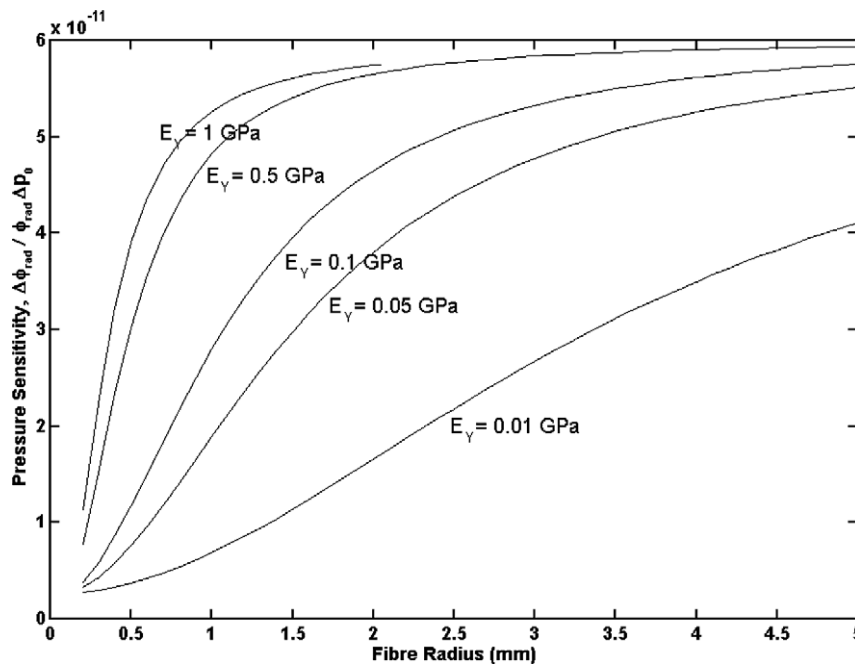


Fig. 23. Calculated pressure sensitivity as a function of fibre radius. The different curves are for outer jacket layers with different Young's moduli, E_Y . The bulk modulus, K_b , was kept the same (4 GPa) in each case.

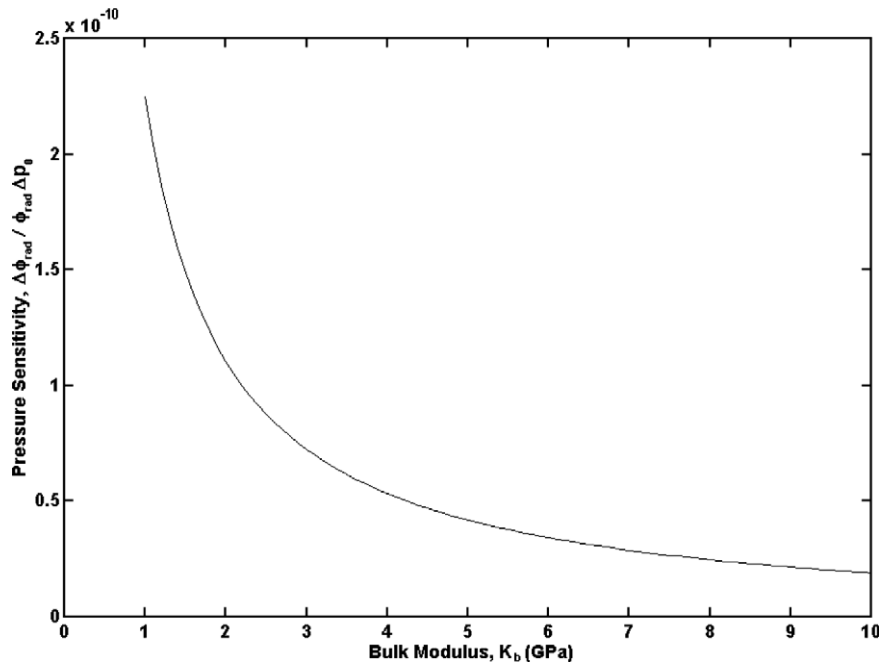


Fig. 24. Calculated pressure sensitivity as a function of bulk modulus, K_b , for a large radius (3 mm) outer jacket. Young's modulus, E_Y , was kept constant (0.1 GPa).

onstrated that fibres with metal cladding layers are much less sensitive than fibres clad with low bulk modulus materials [77,89]. Non-metallised submarine telecommunication cables may be particularly suited to detection by this method.

4. Summary

An experiment was performed to investigate whether a conventional OTDR could be used to detect acoustically-generated stresses within an optic fibre. A change in the back-scattered power in the optical window of the detector was found to occur. In the experiment the change that was observed was very small. It was concluded that an OTDR system, specifically designed to pick out the Brillouin frequency shift, or an interferometric system designed to pick up small changes in optical phase, would be required for the acousto-optic detection approach to work in practice.

The strain dependence of the Brillouin shift was estimated to be around 130 Hz/kPa. At optical wavelengths of around 1 500 nm in glass, this corresponds to a change in the phase of the Brillouin signal of only 10^{-15} Pa^{-1} . For the acousto-optic effect, the change in phase of the optical signal was expected to be significantly larger. The pressure sensitivity was shown to be related to the elastic properties of the fibre jacket material. A greatly enhanced sensitivity is predicted if the cladding has a high compressibility (which is expected to be the case for non-metallised fibre optic cables). For a fibre having a relatively thick and compressible cladding, it was calculated to be of the order of 10^{-10} Pa^{-1} .

The sensitivity values for a real fibre optic cable buried in marine sediment are unknown, although they are expected to be similar to the values predicted (above) for the Brillouin and acousto-optic effects. Therefore, it is surmised that an acoustic pressure amplitude in excess of 100 kPa would be required to be incident on the cable to achieve a measurable effect, given that a sensitivity of around 1 part in 10^7 can be achieved using interferometric techniques. Whilst it may be difficult to generate such pressures at the ranges indicated by Fig. 17 [90], a vehicle close to (or on) the seabed (such as is discussed in the body of the paper) may be more effective at delivering such pressures at the cable. It is therefore conceivable that the techniques discussed in the Appendix could be useful in identifying cables when used as an adjunct to the detection methods discussed in the body of the paper.

References

- [1] Lim R, Lopes JL, Hackman RH, Todoroff DG. Scattering by objects buried in underwater sediments: theory and experiment. *J Acoust Soc Am* 1993;93:1762–1783 .
- [2] Lim R. Scattering by an obstacle in a plane-stratified poroelastic medium: application to an obstacle in ocean sediments. *J Acoust Soc Am* 1994;95:1223–44.
- [3] Heald GJ, Griffiths HD. A review of underwater detection techniques and their applicability to the landmine problem. Second international conference on the detection of abandoned land mines; 1998. p. 173–6.
- [4] Schmidt H, Lee J. Physics of 3-D scattering from rippled seabeds and buried targets in shallow water. *J Acoust Soc Am* 1999;105:1605–17.
- [5] Edwards JR, Schmidt H, LePage K. Bistatic synthetic aperture target detection and imaging with an AUV. *IEEE J Oceanic Eng* 2001;26: 690–9.

- [6] Hetet A, Pigois L, Salaun A, Goh IN, Lim CK, Chia CS. Multiple experimental investigations into buried mines detection and classification with SAS. OCEANS, 2001. MTS/IEEE conference and exhibition, vol. 1; 2001. p. 234–5.
- [7] Tesei A, Lim R, Maguer A, Fox WLJ, Schmidt H. Measurements of acoustic scattering from partially and completely buried spherical shells. *J Acoust Soc Am* 2002;112:1817–30.
- [8] Dugelay S, Brothers R. Controlled seabed clutter fluctuations and their effects on backscattered signal statistics. *Oceans '02 MTS/IEEE*, vol. 1; 2002. p. 1–6.
- [9] Pinto MA, Bellettini A, Hollett R, Tesei A. Real- and synthetic-array signal processing of buried targets. *IEEE J Oceanic Eng* 2002;27:484–94.
- [10] LePage KD, Schmidt H. Bistatic synthetic aperture imaging of proud and buried targets from an AUV. *IEEE J Oceanic Eng* 2002;27:471–83.
- [11] Pinto MA, Bellettini A, Hollett R, Tesei A. High resolution imaging of buried targets. *IEEE J Oceanic Eng* 2002;27:484–94.
- [12] Griffin S, Bradley J, Richardson MD. Improved subsequent burial instrumented mines. *Sea Technol* 2003;44:40–4.
- [13] Nakamura Y, Yamaguchi I, Tanaka, Hama Y. Buried object detection with synthetic aperture sonar. *International symposium on underwater technology* 2004; 2004. p. 27–31.
- [14] Thorne PD, Richardson MD, Griffin S, Traykovski P. Utilisation of the application of high frequency acoustics to sediment processes for mine burial prediction. In: Pace NG, Blondell P, editors. *Proceedings of the conference on boundary influences in high frequency, shallow water acoustics*; 2005. p. 375–82.
- [15] Leighton TG. From seas to surgeries, from babbling brooks to baby scans: the acoustics of gas bubbles in liquids. *Int J Mod Phys B* 2004;18:3267–314.
- [16] Tian WM. Searching and locating of underwater pipelines. In: Pace NG, Blondell P, editors. *Proceedings of the conference on boundary influences in high frequency, shallow water acoustics*; 2005. p. 287–94.
- [17] Schock SG, Tellier A, Wulf J, Sara J, Ericksen M. Buried object scanning sonar. *IEEE J Oceanic Eng* 2001;26:677–89.
- [18] Dix JK, Arnott S, Best AI, Gregory D. The acoustic characteristics of marine archaeological wood. In: Leighton TG, Heald GJ, Griffiths H, Griffiths G, editors. *Acoustical oceanography*, *Proceedings of the Institute of Acoustics*, vol. 23, part 2; 2001. p. 299–305.
- [19] Plets RMK, Dix JK, Adams JR, Best AI, Mindell DA. High resolution acoustic imagery from a shallow archaeological site: the Grace Dieu A case study. In: Papadakis JS, Bjorno L, editors. *Proceedings of the first international conference on underwater acoustic measurements: technologies and results*, vol. 3; 2005. p. 1303–8.
- [20] Leighton TG, Evans RCP. Studies into the detection of buried objects (particularly optical fibres) in saturated sediment. Part 1: introduction. ISVR technical report no. 309; 2007.
- [21] Leighton TG. From sea to surgeries, from babbling brooks to baby scans: bubble acoustics at ISVR. *Proc Inst Acoust* 2004;26(1):357–81.
- [22] Hamilton EL. Compressional-wave attenuation in marine sediments. *Geophysics* 1972;37:620–46.
- [23] Hamilton EL. Acoustic properties of sediments. In: Lara-Saenz A, Ranz Guerra C, Carbofite C, editors. *Acoustics and ocean bottom*, Consejo Superior de Investigaciones Cientificas (CSIC), Madrid; 1987.
- [24] Hamilton EL. Sound attenuation as a function of depth in the sea floor. *J Acoust Soc Am* 1976;59(3):528–35.
- [25] Apel JR. Principles of ocean physics. *International geophysics series*, vol. 38. Academic Press; 1987.
- [26] Leighton TG, Evans RCP. Studies into the detection of buried objects (particularly optical fibres) in saturated sediment. Part 2: design and commissioning of test tank. ISVR technical report no. 310; 2007.
- [27] Hamilton EL. Elastic properties of marine sediments. *J Geophys Res* 1971;76:579–604.
- [28] Pickard GL, Emery WJ. Descriptive physical oceanography: an introduction. 4th (SI) ed. Pergamon Press; 1982. p. 11.
- [29] Nyborg WL, Rudnick I, Schilling HK. Experiments on acoustic absorption in sand and soil. *J Acoust Soc Am* 1950;22:422–5.
- [30] Zhabrodsky SS. Hydrodynamics and heat transfer in fluidised beds. The M.I.T. Press; 1966.
- [31] Buckingham MJ. Theory of acoustic attenuation, dispersion and pulse propagation in granular materials including marine sediments. *J Acoust Soc Am* 1997;102:2579–96.
- [32] Buckingham MJ. Seismic wave propagation in rocks and marine sediments: a new theoretical approach. In: Alippi A, Cannelli GB, editors. *Proceedings of the fourth European conference on underwater acoustics*; 1998. p. 301–6.
- [33] Buckingham MJ. Theory of compressional and shear waves in fluidlike marine sediments. *J Acoust Soc Am* 1998;103:288–99.
- [34] Urlick RJ. Principles of underwater sound. 3rd ed. New York: McGraw-Hill; 1983. p. 75–9 [chapter 4].
- [35] Kinsler LE, Frey AR, Coppens AB, Sanders JV. Fundamentals of acoustics. 3rd ed. Toronto: John Wiley & Sons; 1982. p. 182–5.
- [36] Nielsen RO. Sonar signal processing. Artech House, Inc.; 1991. p. 205–6 [chapter 2].
- [37] Prada C, Wu F, Fink M. The iterative time reversal mirror: a solution to self-focusing in the pulse echo mode. *J Acoust Soc Am* 1991;90:1119–29.
- [38] Skolnik MI. Radar handbook. 2nd ed. McGraw-Hill Publishing Company; 1990.
- [39] Brüel, Kjør, Technical documentation for hydrophone types 8103, 8104, 8105, 8106; 1992.
- [40] Livett AJ, Preston RC. A comparison of the AIUM/NEMA, IEC and FDA (1980) definitions of various acoustic output parameters for ultrasonic transducers. *Ultrasound Med Biol* 1985;11:793–802.
- [41] Evans RCP. Acoustic penetration of the seabed, with particular application to the detection of non-metallic buried cables, PhD thesis, University of Southampton; 1999.
- [42] Ogilvy JA. Theory of wave scattering from random rough surfaces. Bristol: Adam Hilger; 1991.
- [43] Evans RC, Leighton TG. Studies into the detection of buried objects (particularly optical fibres) in saturated sediment. Part 3: experimental investigation of acoustic penetration of saturated sediment. ISVR technical report no. 311; 2007.
- [44] http://www.isvr.soton.ac.uk/fdag/uaua/Sat_Sed_target.htm.
- [45] Williams KL, Jackson DR. Bistatic bottom scattering: model, experiments, and model/data comparison. *J Acoust Soc Am* 1998;103:169–81.
- [46] Evans RC, Leighton TG. An experimental investigation of acoustic penetration into sandy sediments at sub-critical grazing angles. In: Alippi A, Cannelli GB, editors. *Proceedings of the fourth European conference on underwater acoustics*; 1998. p. 697–702.
- [47] Brekhovskikh LM. Waves in layered media. 2nd ed. Academic Press; 1980. p. 48–50 [chapter 1].
- [48] Jackson DR, Ivakin AN. Scattering from elastic sea beds: first-order theory. *J Acoust Soc Am* 1998;103:336–45.
- [49] Brekhovskikh LM, Lysanov YP. Fundamentals of ocean acoustics. 2nd ed. Springer-Verlag; 1991 [chapter 3].
- [50] Buckingham MJ. Wave propagation, stress relaxation and grain-to-grain shearing in saturated, unconsolidated marine sediments. *J Acoust Soc Am* 2000;108:2796–815.
- [51] Ivakin AN. Models of scattering for remote acoustic sensing of the seafloor. In: Leighton TG, Heald GJ, Griffiths H, Griffiths G editors. *Acoustical oceanography*, *Proceedings of the Institute of Acoustics*, vol. 23, part 2; 2001. p. 268–75.
- [52] Briggs KB, Williams KL, Richardson MD, Jackson DR. Effects of changing roughness on acoustic scattering: (1) natural changes. In: Leighton TG, Heald GJ, Griffiths H, Griffiths G, editors. *Acoustical oceanography*, *Proceedings of the Institute of Acoustics*, vol. 23, part 2; 2001. p. 375–83.
- [53] Richardson MD, Briggs KB, Williams KL, Lyons AP, Jackson DR. Effects of changing roughness on acoustic scattering: (2) anthropogenic changes. In: Leighton TG, Heald GJ, Griffiths H, Griffiths G,

- editors. *Acoustical oceanography*, Proceedings of the Institute of Acoustics, vol. 23, part 2; 2001. p. 383–90.
- [54] Williams KL, Jackson DR, Thorsos EI, Tang D, Schock SG. Comparison of sound speed and attenuation measured in a sandy sediment to predictions based on the Biot theory of porous media. *IEEE J Oceanic Eng* 2002;27:413–28.
- [55] Chotiros NP. Biot model of sound propagation in water-saturated sand. *J Acoust Soc Am* 1995;97:199–214.
- [56] Lopes JL. Observations of anomalous acoustic penetration into sediments at shallow grazing angles. *J Acoust Soc Am* 1996;99:2473–500.
- [57] Chotiros NP. Acoustic penetration of ocean sediments in the context of Biot's theory. *J Acoust Soc Am* 1996;99:2474–2500.
- [58] Jackson DR, Moe JE, Thorsos EI, Williams KL. Subcritical penetration of sandy sediments due to interface roughness. *J Acoust Soc Am* 1996;99:2474–500.
- [59] Hickey CJ, Sabatier JM. Choosing Biot parameters for modeling water-saturated sand. *J Acoust Soc Am* 1997;102:1480–4.
- [60] Stoll RD. Comments on 'Biot model of sound propagation in water-saturated sand' *J Acoust Soc Am* 1995;97:199–214. *J Acoust Soc Am* 1998;103:2723–5.
- [61] Chotiros NP. Response to: Comments on 'Biot model of sound propagation in water-saturated sand' *J Acoust Soc Am* 1995;97:199–214. *J Acoust Soc Am* 1998;103:2726–9.
- [62] Thorsos EI, Jackson DR, Moe JE, Williams KL. Modeling of subcritical penetration into sediments due to interface roughness. *SACLANTCEN conference proceedings CP-45, NATO SACLANT undersea research centre*; 1997. p. 563–69.
- [63] Chotiros NP, Smith DE, Piper JN, McCurley BK, Lent K, Crow N, Banks R, Ma H. Acoustic penetration of a sandy sediment. In: Leighton TG, Heald GJ, Griffiths H, Griffiths G, editors. *Acoustical oceanography*. Proceedings of the Institute of Acoustics, vol. 23, part 2; 2001. p. 355–60.
- [64] Pouliquen E, Lyons AP, Pace NG. Penetration of acoustic waves into rippled sandy seafloors. *J Acoust Soc Am* 2000;108:2071–81.
- [65] Maguer A, Fox WLJ, Schmidt H, Pouliquen E, Bovio E. Mechanisms for subcritical penetration into a sandy bottom: experimental and modelling results. *J Acoust Soc Am* 2000;107:1215–26.
- [66] Thorsos EI, Jackson DR, Williams KL. Modeling of subcritical penetration into sediments due to interface roughness. *J Acoust Soc Am* 2000;107:263–77.
- [67] Simpson HJ, Houston BH. Synthetic array measurements of acoustic waves propagating into a water-saturated sandy bottom for a smoothed and roughened interface. *J Acoust Soc Am* 2000;107:2329–37.
- [68] Evans RC, Leighton TG. Studies into the detection of buried objects (particularly optical fibres) in saturated sediment. Part 4: experimental investigations into the acoustic detection of objects buried in saturated sediment, ISVR technical report no. 312; 2007.
- [69] Evans RC, Leighton TG. The detection of cylindrical objects of low acoustic contrast buried in the seabed. In: Kuhl PK, Crum LA, editors. *Proceedings of the 16th international congress on acoustics and 135th meeting of the acoustical society of America (ICA/ASA '98)*; 1998. p. 1369–70.
- [70] Daniels DJ, Gunton DJ, Scott HE. Introduction to subsurface radar. *IEE proceedings*, vol. 135, part F, no. 4; 1988. p. 278–320.
- [71] Press WH, Teukolsky SA, Vetterling WT, Flannery BP. *Numerical recipes in C: the art of scientific computing*. 2nd ed. Cambridge University Press; 1995. p. 547–9 [Section 13.3].
- [72] Malecki I. *Physical foundations of technical acoustics*. Oxford: Pergamon Press; 2000 [chapter 6].
- [73] Cook CE, Bernfeld M. *Radar signals – an introduction to theory and application*. Academic Press; 1967 [chapter 2].
- [74] Hackman RH. *Acoustic scattering from elastic solids*. In: Pierce AD, Thurston RN, editors. *Physical acoustics*, vol. XXII. Academic Press, Inc.; 1993. p. 8.
- [75] Griffiths HD, Shafeeu H, Rafik TA, Meng Z, Cowan CFN, Anthony DK, et al. Interferometric synthetic aperture sonar for high-resolution 3-D mapping of the seabed. *IEE Proc, Radar, Sonar Navigation* 1997;144(2):96–103.
- [76] Leighton TG. From sea to surgeries, from babbling brooks to baby scans: bubble acoustics at ISVR. *Proc Inst Acoust* 2004;26(1):357–81.
- [77] Evans RC, Leighton TG. Studies into the detection of buried objects (particularly optical fibres) in saturated sediment. Part 5: an acousto-optic detection system. ISVR technical report no. 313; 2007.
- [78] Anritsu MW9070A optical time-domain reflectometer operation manual, Anritsu Corporation, 5-10-27, Minami-Azabu, Minato-Ku, Tokyo 106.
- [79] Leighton TG. *The acoustic bubble*. London: Academic Press; 1994. p. 46.
- [80] Leighton TG, Ramble DG, Phelps AD, Morfey CL, Harris PP. Acoustic detection of gas bubbles in a pipe. *Acust Acta Acust* 1998;84:801–14.
- [81] Stolen RH. Nonlinearity in fiber transmission. *Proc IEEE* 1980;68(10):1232–6.
- [82] Hecht E. *Optics*. 2nd ed.. Addison-Wesley Publishing Company; 1987. p. 175.
- [83] Bell J. Scattered light checks health of optical links. *Opto Laser Eur* 1997.
- [84] Nash P. Review of interferometric optical fibre hydrophone technology. *IEE Proc, Radar, Sonar Navigation* 1996;143:204–9.
- [85] Hecht E. *Optics*. 2nd ed. Addison-Wesley Publishing Company; 1987. p. 339–61.
- [86] Timoshenko S. *Theory of elasticity*, engineering societies monographs. New York and London: McGraw-Hill Book Company, Inc.; 1934 [chapter 12].
- [87] Hughes R, Jarzynski J. Static pressure sensitivity amplification in interferometric fiber-optic hydrophones. *Appl Opt* 1980;19:98–107.
- [88] Lagakos N, Schnaus EU, Cole JH, Jarzynski J, Bucaro JA. Optimizing fiber coatings for interferometric acoustic sensors. *IEEE J Quantum Electron* 1982;18(4):683–9.
- [89] Lagakos N, Bucaro JA. Pressure desensitization of optical fibers. *Appl Opt* 1981;20:2716–20.
- [90] Mullins J. Mine smasher. *New Scientist* 1997;2104:11.